# Structure and Drug Binding of the SARS-CoV-2 Envelope Protein in Phospholipid Bilayers

**Mei Hong** ( meihong@mit.edu )
Massachusetts Institute of Technology https://orcid.org/0000-0001-5255-5858
**Venkata Mandala**
Massachusetts Institute of Technology https://orcid.org/0000-0002-6358-0642
**Matthew McKay**
Massachusetts Institute of Technology
**Alexander Shcherbakov**
Massachusetts Institute of Technology https://orcid.org/0000-0002-5728-7175
**Aurelio Dregni**
Massachusetts Institute of Technology
**Antonios Kolocouris**
National and Kapodidtrian University of Athens, Faculty of Pharmacy, Section of Pharmaceutical Chemistry

**Article**

**Keywords:** COVID-19, SARS-CoV-2, envelope protein, drug development, phospholipid bilayers

**Posted Date:** September 24th, 2020

**DOI:** https://doi.org/10.21203/rs.3.rs-77124/v1



**Version of Record:** A version of this preprint was published at Nature Structural & Molecular Biology on November 11th, 2020. See the published version at https://doi.org/10.1038/s41594-020-00536-8.

# Structure and Drug Binding of the SARS-CoV-2 Envelope Protein in Phospholipid Bilayers

Venkata S. Mandala [1], Matthew J. McKay [1], Alexander A. Shcherbakov [1], Aurelio J. Dregni [1], Antonios Kolocouris [2], Mei Hong [1]*

[1] Department of Chemistry, Massachusetts Institute of Technology, Cambridge, Massachusetts, 02139, USA

[2] Department of Pharmaceutical Chemistry, National and Kapodistrian University of Athens, Panepistimioupolis Zografou, Athens 15771, Greece

* Corresponding author: Mei Hong, Professor of Chemistry, email: meihong@mit.edu

September 13, 2020

**Severe acute respiratory syndrome coronavirus 2 (SARS-CoV-2) is the causative agent of the ongoing COVID-19 pandemic. Successful development of vaccines and antivirals against SARS-CoV-2 requires a comprehensive understanding of the essential proteins of the virus. The envelope (E) protein of SARS-CoV-2 assembles into a cation-selective channel that mediates virus budding, release, and host inflammation response. E blockage reduces virus pathogenicity while E deletion attenuates the virus. Here we report the 2.4 Å structure and drug-binding site of E's transmembrane (TM) domain, determined using solid-state nuclear magnetic resonance (NMR) spectroscopy. In lipid bilayers that mimic the endoplasmic reticulum Golgi intermediate compartment (ERGIC) membrane, ETM forms a five-helix bundle surrounding a narrow central pore. The middle of the TM segment is distorted from the ideal α-helical geometry due to three regularly spaced phenylalanine residues, which stack within each helix and between neighboring helices. These aromatic interactions, together with interhelical Val and Leu interdigitation, cause a dehydrated pore compared to the viroporins of influenza and HIV viruses. Hexamethylene amiloride and amantadine bind shallowly to polar residues at the N-terminal lumen, while acidic pH affects the C-terminal conformation. These results indicate that SARS-CoV-2 E forms a structurally robust but bipartite channel whose N- and C-terminal halves can interact with drugs, ions and other viral and host proteins semi-independently. This structure establishes the atomic basis for designing E inhibitors as antiviral drugs against SARS-CoV-2.**

Nine months into the COVID-19 pandemic, no vaccine or antiviral drugs are yet available against SARS-CoV-2, owing to a lack of knowledge about the detailed structures and functions of key virus proteins. The RNA genome of SARS-CoV-2 encodes three membrane proteins: the spike protein, which binds the cell-surface receptor to mediate virus entry; the membrane protein, which contributes to virus assembly and budding [1]; and the envelope protein (**Fig. 1a**). E is a 75-residue viroporin (**Fig. 1b**) that forms a cation-selective channel across the ERGIC membrane [2,3]. The protein mediates the budding and release of progeny viruses [4] and is involved in activation of the host inflammasome [5]. E's channel activity is blocked by hexamethylene amiloride (HMA) [6] and amantadine (AMT) [7], the latter also known to inhibit the viroporins of influenza A virus and HIV-1 [8,9]. E inhibition reduces viral pathogenicity while E deletion gives rise to attenuated viruses in some coronaviruses [10-12], suggesting that E is a potential antiviral and vaccine target.

Despite its importance to SARS-CoV-2 pathogenesis, E's structure, particularly for the ion-conducting TM domain (residues 8-38) [2,13], has been elusive. Sedimentation equilibrium and gel electrophoresis data indicate that the TM domain assembles into a pentamer in detergent micelles such as SDS and perfluorooctanoic acid [3,14,15], but the membrane topology is debated. X-ray scattering of DMPC-bound ETM of SARS-CoV found Phe23 electron density in the lipid headgroup region, suggesting that the TM domain crosses the lipid bilayer twice as a short hairpin [16], thus juxtaposing the N-terminal Glu8 with the C-terminal Arg38. In contrast, solution NMR studies of E bound to DPC [10], SDS [15], and LMPG [17] micelles indicate a single-span TM helix; however, the pore-facing residues and the pentameric assembly have not been well established.

To avoid potential structural distortion caused by detergents, we determined the ETM structure in phospholipid bilayers using solid-state NMR spectroscopy. We reconstituted ETM into an ERGIC-mimetic lipid membrane containing phosphocholine, phosphoethanolamine, phosphatidylinositol, phosphoserine and cholesterol. For comparison, we also incorporated the protein into dimyristoylphosphocholine (DMPC) : dimyristoyl-phosphoglycerol (DMPG) membranes. ETM was expressed in *E. coli* using a $His_6$-SUMO fusion tag (**Fig. S1**) and purified by nickel affinity column chromatography and reverse-phase HPLC. One-dimensional (1D) $^{13}C$ and $^{15}N$ NMR spectra of the protein in ERGIC and DMPC : DMPG membranes show temperature-insensitive high

intensities (**Fig. S2a, b**), indicating that the protein is immobilized in the lipid membranes at ambient temperature. Two-dimensional (2D) $^{15}$N-$^{13}$C and $^{13}$C-$^{13}$C correlation spectra show well-resolved peaks for most residues (**Fig. 1c, d**) with $^{13}$C and $^{15}$N linewidths of 0.5 ppm and 0.9 ppm, indicating that the protein conformation is highly homogeneous. We assigned the chemical shifts using 3D correlation NMR experiments (**Fig. S3a, Table S1**). These chemical shifts indicate that residues 14–34 form the α-helical core of the TM domain (**Fig. S3b, c**). Comparison of spectra between the two membranes and at different temperatures (**Fig. S2d-f**) indicate that the N-terminal segment (residues E8-I13) is dynamic at high temperature but has α-helical propensity, while the C-terminal segment (residues T35-R38) is more rigid but displays temperature-dependent conformations. Acidic pH perturbed the chemical shifts of C-terminal residues L34-R38 (**Fig. S4**), supporting the conclusion that the C-terminal segment is conformationally plastic.

The temperature insensitivity of the protein spectra suggests that ETM is oligomerized in lipid bilayers. To determine the oligomeric structure, we prepared two mixed labeled protein samples to measure intermolecular distances. An equimolar $^{13}$C-labeled protein mixed with 4-$^{19}$F-Phe labeled protein (**Fig. S1e**) was used to measure intermolecular $^{13}$C-$^{19}$F distances using the REDOR technique [18] (**Fig. 2a**). ETM contains three regularly spaced phenylalanine (Phe) residues, Phe20, Phe23 and Phe26, at the center of the TM segment. 1D and 2D $^{13}$C NMR spectra were measured without and with $^{19}$F pulses. The resulting difference spectra show the signals of carbons that are in close proximity to a fluorinated Phe on a neighboring helix (**Fig. 2b, Fig. S5a-c**). As expected, residues V17 to L31 are affected by 4-$^{19}$F-Phe, while residues I13 to S16 and A36 to R38 show no REDOR dephasing. Moreover, the three Phe's display two resolved $^{19}$F chemical shifts, indicating that one of the residues has a distinct sidechain conformation. A 2D $^{13}$C-$^{19}$F correlation spectrum (**Fig. 2c**) shows a cross peak between the -118 ppm $^{19}$F signal and A22 Cβ, indicating that this -118 ppm peak is due to either F20 or F23. The -113 ppm $^{19}$F peak shows strong cross peaks with aromatic and numerous aliphatic $^{13}$C chemical shifts. Since F20 and F26 are too far away from each other to form intermolecular contacts, the -118 ppm $^{19}$F peak must be assigned to F20, while F23 and F26 resonate at -113 ppm. To constrain the interhelical packing at the two termini of the TM domain, we prepared a $^{13}$C and $^{15}$N mixed labeled sample, and measured 2D NHHC correlation spectra, which exhibit $^{15}$N-$^{13}$C correlation peaks that are exclusively intermolecular (**Fig. 2d**). These experiments together yielded 35 interhelical $^{13}$C-$^{19}$F distance restraints and 52 interhelical $^{15}$N-$^{13}$C correlations, which are crucial for determining the oligomeric structure of ETM.

To further constrain the E channel architecture, we measured the water accessibilities of different residues using water-edited 2D $^{15}$N-$^{13}$C correlation experiments (**Fig. 2e, Fig. S5d**) [19,20]. Water $^{1}$H magnetization transfer is the highest to the N-terminal residues, the least to the central residues L17 to A32, and moderate to the C terminus (**Fig. 2f**). Thus, the hydration gradient of the protein is primarily along the bilayer normal. The preferential hydration of the N-terminus is especially manifested by the high water-transferred intensity of L19 compared to T30, despite favorable chemical exchange to the Thr sidechain. For the dehydrated center of the TM domain, L28 and V25 show higher hydration than their neighboring residues, suggesting that these residues face the pore. A complementary lipid-edited experiment (**Fig. 2g**) showed much higher intensities for the Phe sidechain carbons than the corresponding water-transferred intensities, indicating that the Phe's are more lipid-facing. The ERGIC-bound ETM shows two-fold lower water accessibility than the closed state of influenza BM2 at the same neutral pH (**Fig. 2f**).

We calculated the structure of ETM using the measured 56 ($\phi$, $\psi$) torsion angles, 87 interhelical distance restraints (**Tables S2, S3**), and 196 intrahelical $^{13}$C-$^{13}$C contacts obtained from 250 ms $^{13}$C spin diffusion spectra (**Fig. S6**) [21]. We disambiguated the direction of interhelical contacts from one helix to the two neighboring helices by considering the pore- versus lipid-facing positions of

the residues, the helical distortion between F20 and F23 (**Fig. S3b**), and the interhelical $^{13}C$-$^{19}F$ Phe-Phe contacts (**Fig. S7e**). The lowest-energy structure ensemble, with a heavy-atom RMSD of 2.4 Å (**Table 1**), shows a long and tight five-helix bundle with a vertical length of ~35 Å for residues V14-L34. The channel diameter varies from 11 Å to 14 Å, based on the Cα-Cα distances between helices *i* and *i*+2 for pore-facing residues (**Fig. 3a)**. The helical bundle is primarily left-handed, although a minor conformer of right-handed bundle is also seen. Each helix is tilted by an angle of about 10˚ from the bilayer normal (**Fig. 3b**); however, this orientation is not uniform, because the helix is not ideal, and exhibits a significant rotation angle change, or twist, between residues F20-F23 [10,17]. The pore of the channel is occupied by mostly hydrophobic residues, including N15, L18, L21, V25, L28, A32 and T35 (**Fig. 3b-d, Fig. S8a**), explaining the poor hydration of the protein. The N-terminus pore is constricted by N15, which forms interhelical sidechain hydrogen bonds (**Fig. 3g**) [22]. Mutation of N15, as well as V25, is known to abolish cation conduction [13]. The helix-helix interface is stabilized by aromatic stacking of F23 and F26 (**Fig. 3e, g**) and van der Waals packing among methyl-rich residues such as the V29-L31-I33 triad (**Fig. 3f**). These extensive hydrophobic interactions create a tighter helical bundle than the influenza viroporin BM2 and the HIV-1 viroporin Vpu (**Fig. S8b**).

To investigate how the E pentamer interacts with drugs, we measured the chemical shifts of the protein in the presence of HMA and AMT. At a drug : protein molar ratio of 4 : 1, HMA caused significant chemical shift perturbations (CSPs) to N-terminal residues, including T9, G10, T11, I13 and S16, followed by modest CSPs for the C-terminal A36 and L37 (**Fig. 4a-c**). This trend is consistent with the micelle data [10,17], but the CSPs in bilayers are much larger than in micelles, with the N-terminal $^{9}$TGT$^{11}$ triplet giving CSPs of 0.35–0.70 ppm. Moreover, in bilayers CSPs were observed at only 4-fold drug excess, while in micelles CSPs were observed at higher drug excesses of 10 to 31-fold [10,17]. The higher sensitivity to drug in lipid bilayers suggests that the bilayer-bound protein conformation is more native. Docking based on these CSPs found that HMA intercalates shallowly into the N-terminal lumen with a distribution of orientations (**Fig. 4d, Fig. S9**), suggesting a dynamic binding mode where HMA exchanges between multiple helices and inhibits cation conduction by steric occlusion of the pore. Within the ensemble of docked structures, more HMA molecules point the guanidinium into the pore and the hexamethylene ring to the lipid headgroups than the reverse orientation. AMT caused smaller CSPs than HMA (**Fig. 4c, Fig. S10a, b**), but the site of binding remains at the N-terminus. Using the 3-$^{19}F$ probe on the adamantane, we measured protein-drug proximities using $^{13}C$-$^{19}F$ REDOR. The spectra showed modest dephasing for the N-terminal N15 and C-terminal I33 (**Fig. S10c-e**), in qualitative agreement with the observed CSPs. The larger CSPs of HMA than AMT are consistent with the micromolar $EC_{50}$ reported for the HCoV-229E E protein [6] compared to the millimolar binding affinities of AMT to SARS-CoV-2 E [7].

Which structural features of this ETM pentamer might be responsible for cation conduction? The N-terminal part of ETM contains a conserved $(E/D/R)_1x(G/A)_3xxhh(N/Q)_8$ motif (**Fig. 1b**), where h is a hydrophobic residue. The most exposed residue, E8, belongs to a dynamic N-terminus whose residues (e.g. T9 and G10) manifest intensities only at high temperature (**Fig. S2d-f**). The E8 sidechain carboxyl is deprotonated at neutral pH and protonated at acidic pH, as seen in the $^{13}C$ chemical shifts (**Fig. S2c**). We hypothesize that the protonation equilibria of this loose ring of E8 quintet, together with the anionic lipids in the ERGIC membrane, may regulate the ion selectivity of ETM at the channel entrance. A ring of negatively charged Glu residues has been observed as selectivity filters in the hexameric $Ca^{2+}$-selective Orai channels [23] and designed $K^+$ channels [24]. The third residue of the motif, G10, is conserved among coronaviruses to be small and flexible, thus permitting N-terminus motion. The last residue of the motif, N15, is conserved to be either Asn or Gln, whose polar sidechains can coordinate ions as well as forming interhelical hydrogen bonds to stabilize the channel [22]. At the C-terminal end, the conserved small residues A32 and

T35 provide an open cavity for ions. In contrast to these small polar residues, the central portion of the TM domain contains four layers of hydrophobic residues, L18, L21, V25 and L28, which narrow the pore radius to ~2 Å (**Fig. 3d**). This narrow pore can only permit a single file of water molecules or ions, thus partially dehydrating any ions that move through the pore. Thus, the structure shown here may represent the closed state of SARS-CoV-2 E, while the open state may have a larger and more hydrated pore. We note, however, that narrow pores with multiple hydrophobic layers have been observed in ion channels, including the tetrameric $K^+$ channel TMEM175 [25] and the pentameric bestrophin channels [26,27]. Thus, it is possible to achieve charge stabilization and ion selectivity in such a hydrophobic environment, although the detailed mechanisms remain to be understood.

The bilayer-bound structure of SARS-CoV-2 E has similarities as well as differences from the micelle-bound structure [10,17]. In micelles, ETM helix also displays a kink and the N-terminus is similarly disordered, but the handedness of the helical bundle and the identity of pore-facing residues vary with the detergent. For example, in LMPG micelles, F26 and T30 point to the lumen rather than lipids. Thus, the membrane-mimetic environment appears to influence E's oligomeric structure. Compared to influenza and HIV-1 viroporins, the SARS-CoV-2 E helical bundle is tighter and more rigid. AM2 and BM2's TM domains have a higher percentage of polar residues such as His and Ser. As a result, M2 forms wider and more hydrated pores (**Fig. S8b**) [9,28]. The HIV-1 Vpu TM domain has a similarly high percentage of hydrophobic residues as SARS-CoV-2 E, but forms a shorter (~20 Å vertical length) pentameric helical bundle with more tilted helices (~20˚) [29,30]. The E helical bundle is more immobilized than M2 and Vpu [31], and does not undergo whole-body fast uniaxial rotation at high temperatures in DMPX membranes (**Fig. S2**). This immobilization suggest that the protein may interact extensively with lipids. Finally, the helix distortion at F20-F23 may cause the two halves of E's TM domain to respond independently to environmental factors such as pH, membrane composition [16], and other viral and host proteins.

This membrane-bound ETM structure suggests that small-molecule E inhibitors should bind with high affinity to both the acidic E8 and the polar N15 in order to occlude the N-terminal entrance of the protein. The membrane topology of SARS-CoV-2 E is now recognized to be $N_{lumen} – C_{cyto}$ based on antibody-detected selective permeabilization assays [32] and glycosylation data [33]. This orientation would prime the protein to conduct $Ca^{2+}$ out of the ERGIC lumen to activate the host inflammasome [5]. Thus, small-molecule drugs should ideally be targeted and delivered to the ERGIC and Golgi of host cells to maximally inhibit SARS-CoV-2 E [34].

**Main References**


1 Weiss, S. R. & Navas-Martin, S. Coronavirus pathogenesis and the emerging pathogen severe acute respiratory syndrome coronavirus. *Microbiol. Mol. Biol. Rev.* **69**, 635-664, (2005).

2 Wilson, L., McKinlay, C., Gage, P. & Ewart, G. SARS coronavirus E protein forms cation-selective ion channels. *Virology* **330**, 322-331, (2004).

3 Parthasarathy, K. *et al.* Expression and purification of coronavirus envelope proteins using a modified β-barrel construct. *Protein Expr. Purif.* **85**, 133-141, (2012).

4 Schoeman, D. & Fielding, B. C. Coronavirus envelope protein: current knowledge. *Virol. J.* **16**, 69, (2019).

5 Nieto-Torres, J. L. *et al.* Severe acute respiratory syndrome coronavirus E protein transports calcium ions and activates the NLRP3 inflammasome. *Virology* **485**, 330-339, (2015).

6 Wilson, L., Gage, P. & Ewart, G. Hexamethylene amiloride blocks E protein ion channels and inhibits coronavirus replication. *Virology* **353**, 294-306, (2006).

7 Torres, J. *et al.* Conductance and amantadine binding of a pore formed by a lysine-flanked transmembrane domain of SARS coronavirus envelope protein. *Protein Sci.* **16**, 2065-2071, (2007).

8 Hong, M. & DeGrado, W. F. Structural basis for proton conduction and inhibition by the influenza M2 protein. *Protein Sci.* **21**, 1620-1633, (2012).

9 Cady, S. D. *et al.* Structure of the amantadine binding site of influenza M2 proton channels in lipid bilayers. *Nature* **463**, 689-692, (2010).

10 Pervushin, K. *et al.* Structure and inhibition of the SARS coronavirus envelope protein ion channel. *PLoS Pathog.* **5**, e1000511, (2009).

11 DeDiego, M. L. *et al.* A severe acute respiratory syndrome coronavirus that lacks the E gene is attenuated in vitro and in vivo. *J. Virol.* **81**, 1701-1713, (2007).

12 Nieto-Torres, J. L. *et al.* Severe acute respiratory syndrome coronavirus envelope protein ion channel activity promotes virus fitness and pathogenesis. *PLoS Pathog.* **10**, e1004077, (2014).

13 Verdiá-Báguena, C. *et al.* Coronavirus E protein forms ion channels with functionally and structurally-involved membrane lipids. *Virology* **432**, 485-494, (2012).

14 Torres, J., Wang, J., Parthasarathy, K. & Liu, D. X. The transmembrane oligomers of coronavirus protein E. *Biophys. J.* **88**, 1283-1290, (2005).

15 Li, Y., Surya, W., Claudine, S. & Torres, J. Structure of a conserved Golgi complex-targeting signal in coronavirus envelope proteins. *J. Biol. Chem.* **289**, 12535-12549, (2014).

16 Arbely, E. *et al.* A highly unusual palindromic transmembrane helical hairpin formed by SARS coronavirus E protein. *J. Mol. Biol.* **341**, 769-779, (2004).

17 Surya, W., Li, Y. & Torres, J. Structural model of the SARS coronavirus E channel in LMPG micelles. *Biochim. Biophys. Acta* **1860**, 1309-1317, (2018).

18 Gullion, T. & Schaefer, J. Rotational echo double resonance NMR. *J. Magn. Reson.* **81**, 196-200, (1989).

19 Dregni, A. J. *et al.* In vitro 0N4R tau fibrils contain a monomorphic beta-sheet core enclosed by dynamically heterogeneous fuzzy coat segments. *Proc. Natl. Acad. Sci. U.S.A.* **116**, 16357-16366, (2019).

20 Williams, J. K. & Hong, M. Probing membrane protein structure using water polarization transfer solid-state NMR. *J. Magn. Reson.* **247**, 118-127, (2014).

21 Schwieters, C. D., Kuszewski, J. J., Tjandra, N. & Clore, G. M. The Xplor-NIH NMR molecular structure determination package. *J. Magn. Reson.* **160**, 65-73, (2003).

22 Choma, C., Gratkowski, H., Lear, J. D. & DeGrado, W. F. Asparagine-mediated self-association of a model transmembrane helix. *Nat. Struc. Biol.* **7**, 161-166, (2000).
23 Hou, X., Pedi, L., Diver, M. M. & Long, S. B. Crystal structure of the calcium release-activated calcium channel Orai. *Science* **338**, 1308-1313, (2012).
24 Xu, C. *et al.* Computational design of transmembrane pores. *Nature* **585**, 129-134, (2020).
25 Lee, C. *et al.* The lysosomal potassium channel TMEM175 adopts a novel tetrameric architecture. *Nature* **547**, 472-475, (2017).
26 Kane Dickson, V., Pedi, L. & Long, S. B. Structure and insights into the function of a Ca(2+)-activated Cl(-) channel. *Nature* **516**, 213-218, (2014).
27 Yang, T. *et al.* Structure and selectivity in bestrophin ion channels. *Science* **346**, 355-359, (2014).
28 Mandala, V. S., Loftis, A. R., Shcherbakov, A. A., Pentelute, B. L. & Hong, M. Atomic structures of closed and open influenza B M2 proton channel reveal the conduction mechanism. *Nat. Struct. Mol. Biol.* **27**, 160-167, (2020).
29 Park, S. H. *et al.* Three-dimensional structure of the channel-forming trans-membrane domain of virus protein "u" (Vpu) from HIV-1. *J. Mol. Biol.* **333**, 409-424, (2003).
30 Lu, J. X., Sharpe, S., Ghirlando, R., Yau, W. M. & Tycko, R. Oligomerization state and supramolecular structure of the HIV-1 Vpu protein transmembrane segment in phospholipid bilayers. *Protein Sci.*, (2010).
31 Cady, S. D., Goodman, C., Tatko, C. D., DeGrado, W. F. & Hong, M. Determining the orientation of uniaxially rotating membrane proteins using unoriented samples: a 2H, 13C, AND 15N solid-state NMR investigation of the dynamics and orientation of a transmembrane helical bundle. *J. Am. Chem. Soc.* **129**, 5719-5729, (2007).
32 Nieto-Torres, J. L. *et al.* Subcellular location and topology of severe acute respiratory syndrome coronavirus envelope protein. *Virology* **415**, 69-82, (2011).
33 Duart, G. *et al.* SARS-CoV-2 envelope protein topology in eukaryotic membranes. *Open Biol.* **10**, 200209, (2020).
34 Abramson, A. *et al.* An ingestible self-orienting system for oral delivery of macromolecules. *Science* **363**, 611-615, (2019).

**Table 1**. Structure calculation and refinement statistics for ERGIC-membrane bound ETM.

| | |
|---|---|
| **NMR distance and dihedral constraints** | |
| Distance constraints | |
| Total NOE | 283 × 5 |
| Inter-residue | 283 × 4 |
| Sequential ($\|i - j\| = 1$) | 125 × 5 |
| Medium range ($2 \leq \|i - j\| \leq 4$) | 71 × 5 |
| Long range ($\|i - j\| \geq 5$) | 0 × 5 |
| Intermolecular | 87 × 5 |
| Total dihedral-angle restraints | |
| $\phi$ | 28 × 5 |
| $\psi$ | 28 × 5 |
| Total orientation constraints | 0 × 5 |
| $^{1}H$-$^{15}N$ dipolar couplings | 0 × 5 |
| Hydrogen bond restraints | 11 × 5 |
| **Structure statistics** | |
| Violations (mean ± s.d.) | |
| Distance constraints (Å) | 0.18 ± 0.09 |
| Dihedral-angle constraints (°) | 0.62 ± 0.22 |
| Max. dihedral-angle violation (°) | 6.52 |
| Max. distance-constraint violation (Å) | 1.64 |
| Deviations from idealized geometry | |
| Bond lengths (Å) | 0.004 ± 0.001 |
| Bond angles (°) | 0.47 ± 0.06 |
| Impropers (°) | 0.34 ± 0.04 |
| Average pairwise r.m.s. deviation (Å) | |
| Heavy atom (residues 10-36) | 2.43 ± 0.75 |
| Backbone (residues 10-36) | 2.08 ± 0.83 |

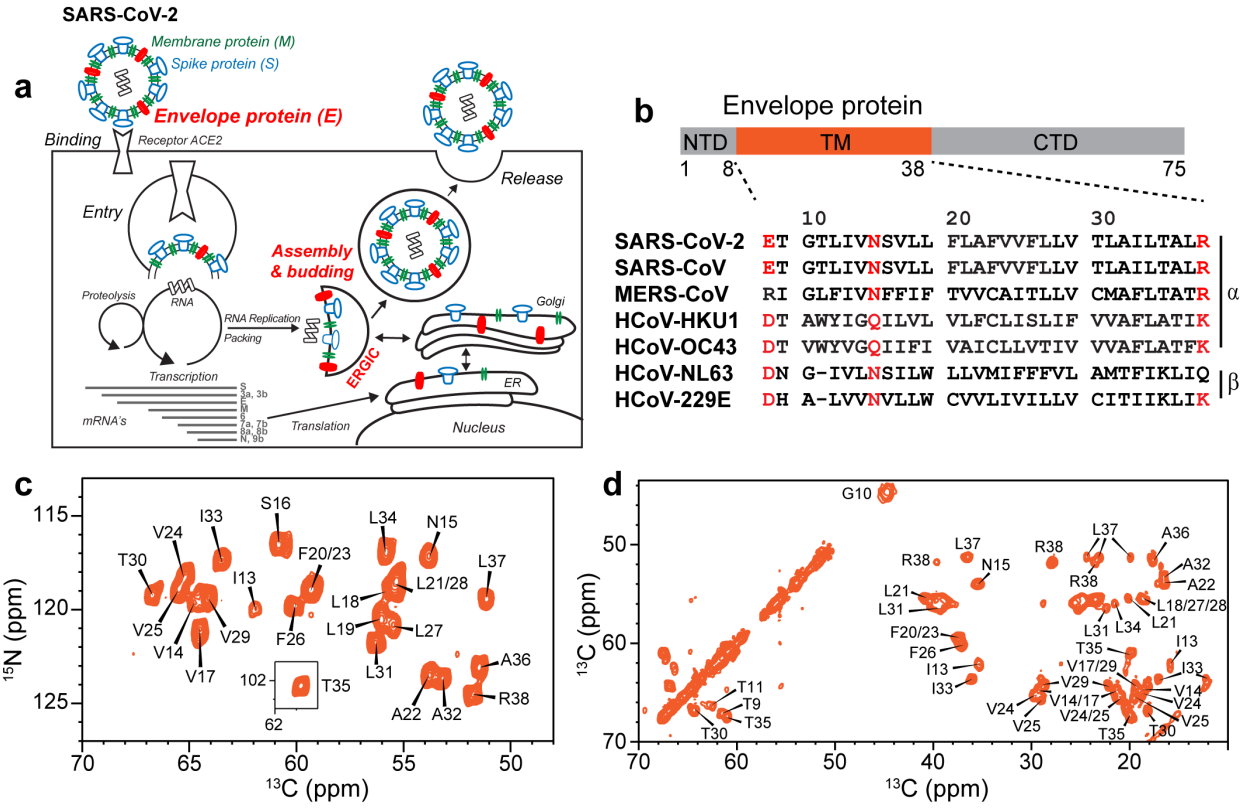


**Figure 1**. Function, sequence, and fingerprint NMR spectra of the SARS-CoV-2 envelope protein. (**a**) E mediates the budding and release of SARS-CoV-2 from the host cell ERGIC lumen and forms a cation-selective channel. (**b**) Sequence domains of E and sequence alignment of the transmembrane segment of E of SARS-CoV-2 with other human-infecting coronaviruses. Key conserved polar residues are shown in red. (**c**) 2D $^{15}$N-$^{13}$Cα correlation spectrum and (**d**) 2D $^{13}$C-$^{13}$C spectrum of ERGIC-membrane bound ETM. The spectra, measured at ambient temperature, show predominantly α-helical chemical shifts, and have high sensitivity and resolution, indicating that the ETM helical bundle is rigid and ordered in the ERGIC-mimetic lipid bilayer.

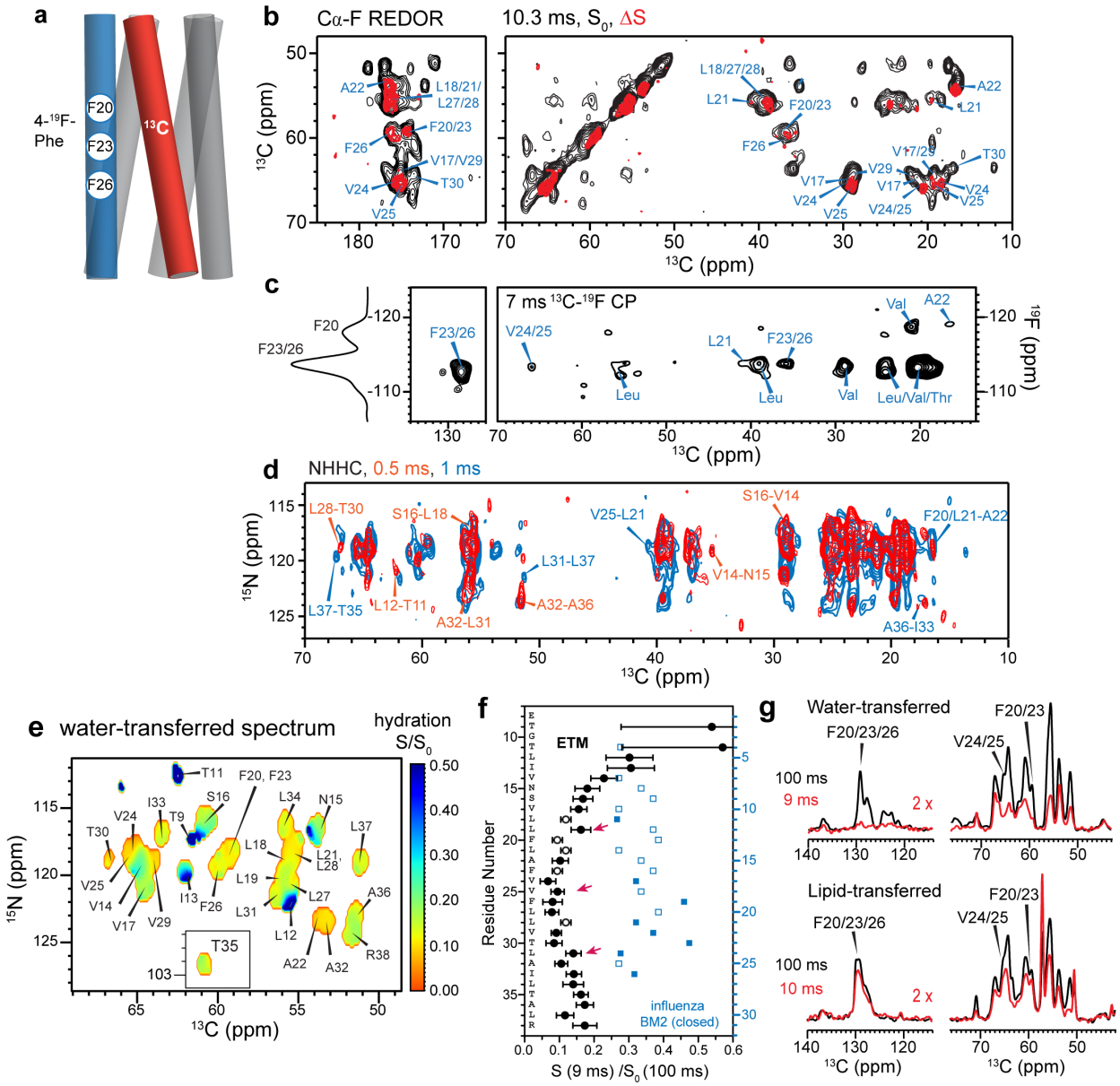


**Figure 2**. Determination of interhelical distances and water accessibility of membrane-bound ETM. (**a**) Schematic of mixed 4F-Phe and $^{13}$C-labeled ETM in a five-helix bundle. (**b**) 2D $^{13}$Cα-F REDOR spectra of ERGIC-membrane bound ETM. The REDOR mixing time was 10.3 ms. The difference spectrum (*orange*) shows residues that are close to the fluorines. (**c**) 2D $^{13}$C-$^{19}$F correlation spectrum allows assignment of the -118 ppm peak to F20 due to a cross peak with A22, while the -113 ppm peak is assigned to F23/F26 based on correlations with F23, F26, and V24/V25. A 1D $^{1}$H-$^{19}$F CP spectrum is overlaid on the left. (**d**) 2D NHHC correlation spectrum of mixed $^{13}$C and $^{15}$N labeled ETM, measured using 0.5 ms (*red*) and 1 ms (*black*) $^{1}$H mixing. All peaks arise from interhelical contacts. Selected assignments are given. **(e)** Residue-specific water accessibilities of ERGIC-bound ETM, obtained from the intensity ratios of water-edited spectra measured with 9 ms and 100 ms $^{1}$H mixing. Higher values (*blue*) indicate higher water accessibility. (**f**) Residue-specific N-Cα cross peak intensity ratios in the 9 ms and 100 ms water-edited spectra of ETM (black). Closed and open circles indicate resolved and overlapped peaks, respectively. For comparison, the water-edited intensities for the high-pH closed state of the influenza BM2 channel (blue squares) are much higher, indicating that the ETM pore is drier than

the BM2 pore. (**g**) Water-edited and lipid-edited 1D $^{13}C$ spectra of ERGIC-membrane bound ETM. The Phe signals are high in the lipid-edited spectra but very low in the water-edited spectra, indicating that the three Phe residues are poorly hydrated and point to the lipids or the helix-helix interface.

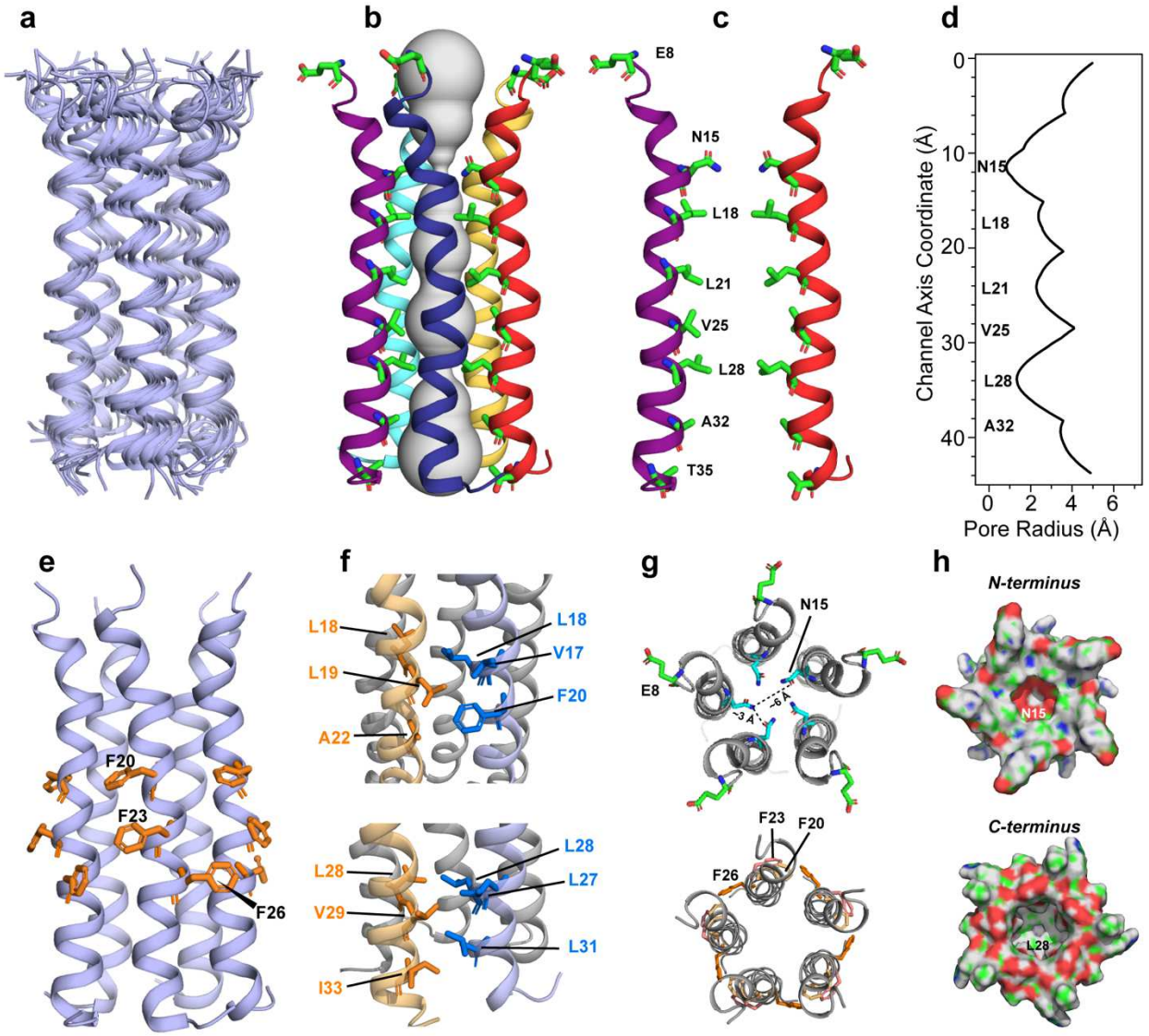


**Figure 3.** Structure of the SARS-CoV-2 envelope protein TM domain in ERGIC-mimetic lipid bilayers. **(a)** Ensemble of the ten lowest-energy structures. (**b**) Sideview of the lowest-energy structure along with pore water (gray), depicted using the HOLE program. Pore-lining residues are shown in sticks. (**c**) Simplified view showing two helices (*i* and *i*+2) with the pore-facing residues. (**d**) Pore radius of ETM obtained from the HOLE program. (**e**) Sideview of the pentamer, displaying the Phe triplet in the middle of the TM segment. (**f**) Two clusters of methyl-interdigitating Leu, Ile and Val residues, stabilizing the helix-helix interface. (**g**) Top views of the disordered N-terminal E8, the pore-occluding N15, and the three Phe residues bridging the helix-helix interface. (**h**) Surface plots of the pentamer, showing that the N-terminal vestibule is slightly tighter than the C-terminal opening.

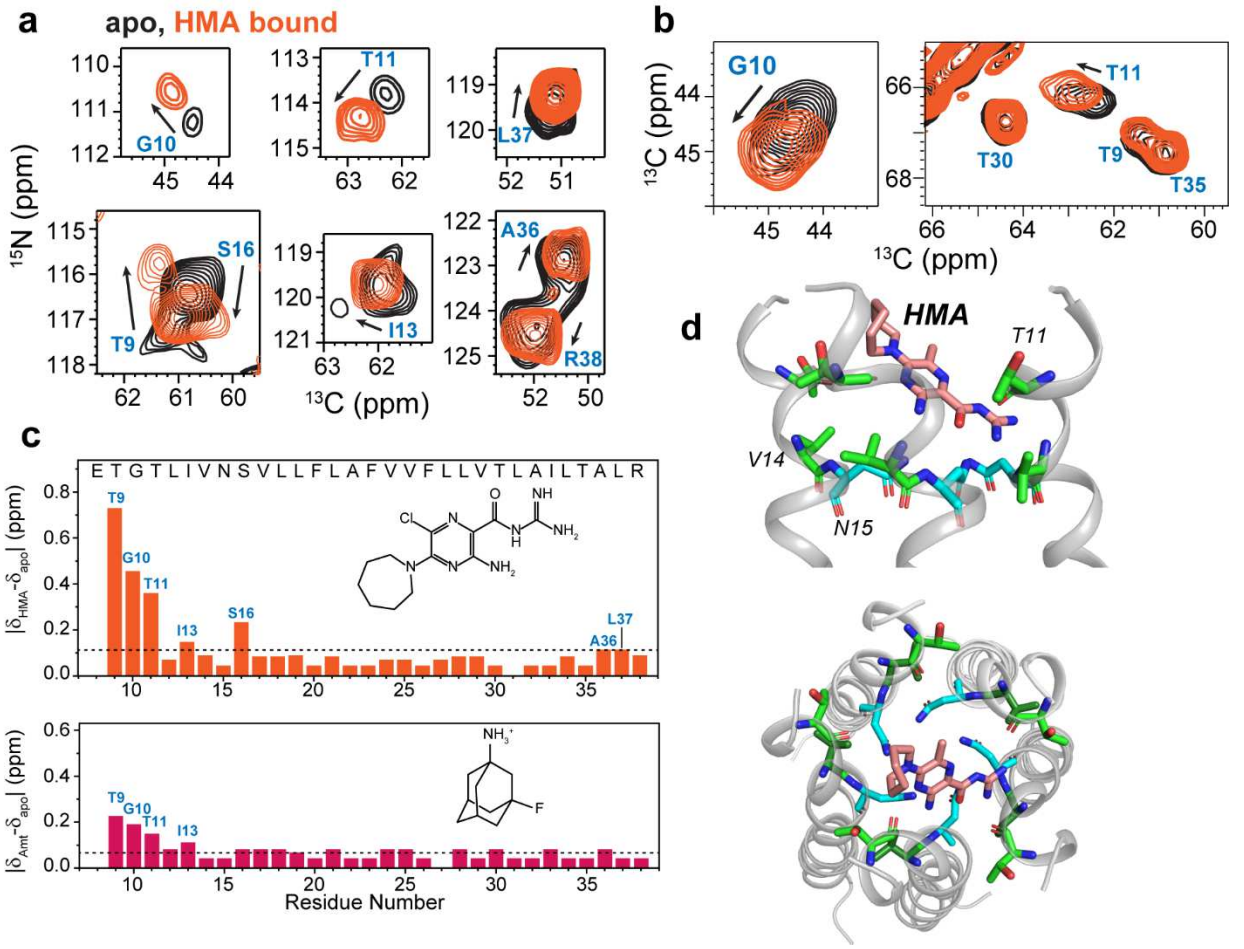


**Figure 4**. Effects of drug binding to ETM in DMPC : DMPG membranes. (**a**) 2D $^{15}$N-$^{13}$Cα correlation spectra of the apo (*black*) and HMA-bound ETM (*orange*), showing chemical shift perturbations by HMA. (**c**) 2D $^{13}$C-$^{13}$C correlation spectra, showing similar CSPs by HMA. (**c**) Per-residue chemical shift perturbations induced by HMA and AMT. N-terminal residues are the most perturbed by both drugs, and HMA causes larger perturbation than AMT. Dashed lines indicate the average CSPs. (**d**) A representative docking pose of HMA. The drug binds to the N-terminal vestibule, with the guanidinium group interacting with T11.

## Methods

### *Cloning of recombinant ETM(8-38)*

The gene encoding the full-length SARS-CoV-2/Wuhan-Hu-1 envelope (E) protein (NCBI reference sequence YP_009724392.1, residues 1-75) was purchased from Genewiz. The gene encoding the TM domain (residues 8-38, ETGTLIVNSVLLFLAFVVFLLVTLAILTALR) was isolated using PCR and cloned into a Champion pET-SUMO plasmid (Invitrogen). The plasmid was transfected into *E. coli* BL21 (DE3) cells (Invitrogen) to express the SUMO-ETM fusion protein containing an N-terminal $His_6$ tag (**Fig. S1a**). The construct's DNA sequence was verified by Sanger sequencing (Genewiz).

### *Expression and purification of $^{13}C$, $^{15}N$-labeled ETM*

A glycerol cell swab stored at -70°C was used to start a 10 mL LB culture containing 50 µg/mL kanamycin. The starter culture was used to inoculate 2 L of LB media. Cells were grown at 37°C until an $OD_{600}$ of 0.6-0.8 and were harvested by centrifugation for 10 minutes at 20°C and 4,400x g. These LB cells were resuspended in 1 L of M9 media (pH 7.8, 48 mM $Na_2HPO_4$, 22 mM $KH_2PO_4$, 8.6 mM NaCl, 4 mM $MgSO_4$, 0.2 mM $CaCl_2$, 50 mg kanamycin) containing 1 g/L $^{15}N$-$NH_4Cl$. The cells were incubated in M9 media for 30 min at 18°C, then 1 g/L U-$^{13}C$ glucose dissolved in 5 mL sterile $H_2O$ and 3 mL 100x MEM vitamins were added. The cells were grown for another 30 min, then protein expression was induced by addition of 0.4 mM isopropyl β-D-1-thiogalactopyranoside (IPTG) along with 2 g/L U-$^{13}C$ glucose in 10 mL sterile $H_2O$. Additional IPTG was added after 1 hour to bring the final concentration to 0.8 mM. Protein expression proceeded overnight for 16 hours at 18°C, reaching an $OD_{600}$ of 2.5.

The cells were spun down at 4°C and 5,000 rpm for 10 min and resuspended in 35 mL Lysis Buffer I (pH 8.0, 50 mM Tris-HCl, 100 mM NaCl, 1.0% Triton X-100, 0.5 mg/mL lysozyme, 10 µL benozonase nuclease, 1 mM $Mg^{2+}$, 10 mM imidazole). Cells were lysed at 4°C by sonication (5 sec on and 5 sec off) for 1 hour using a probe sonicator. The soluble fraction of the cell lysate was separated from the inclusion bodies by centrifugation at 17,000x g for 20 min at 4°C. The supernatant was loaded onto a gravity-flow chromatography column containing ~6 mL nickel affinity resin (Profinity IMAC, BioRad) pre-equilibrated with Lysis Buffer I. The fractions were bound to the resin for 1 hour by gentle rocking at 4°C. The column was washed with 50 mL of Wash Buffer I (pH 8.0, 50 mM Tris-HCl, 100 mM NaCl, 0.1% n-dodecyl-B-D-maltoside (DDM), 30 mM imidazole). SUMO-ETM was eluted with 10-15 mL Elution Buffer (pH 8.0, 50 mM Tris-HCl, 100 mM NaCl, 0.1% DDM, 250 mM Imidazole) (**Fig. S1b**). The eluted protein was diluted to one-third of the original concentration by adding twice the elution volume of Dilution Buffer (pH 8.0, 50 mM Tris-HCl, 100 mM NaCl, 0.1% DDM) to reduce the imidazole concentration before protease cleavage. Approximately 20% of the protein was also found in the insoluble membrane and inclusion body fraction. To purify this fraction, the pelleted mass was resuspended in Lysis Buffer II (Lysis buffer I with added 6 M urea) and rocked gently at 4°C overnight. Soluble protein was isolated by centrifugation at 17,000x g for 20 min at 4°C. Nickel affinity column chromatography proceeded as described above for the soluble fraction, except that Wash Buffer II (Wash Buffer I with added 3 M urea) was utilized in place of Wash Buffer I.

The purified SUMO-ETM fusion protein from both the soluble and inclusion body fractions were cleaved by addition of 1 : 10 (w/w) SUMO protease : SUMO-ETM and 5 mM tris(2-carboxyethyl)phosphine (TCEP) for 2 hours at room temperature with gentle rocking. The cleavage efficiency was assessed by analytical HPLC and was typically ~75%. ETM was purified using preparative RP-HPLC on a Varian ProStar 210 System using an Agilent C3 column (5 µm particle size, 21.2 mm × 150 mm). The protein was eluted using a linear gradient of 5-99% (9:1,

acetonitrile : isopropanol) : water containing 0.1% trifluoroacetic acid over 35 minutes at a flow rate of 10 mL/min (**Fig. S1c**). The purified protein was dried down to a film under a stream of nitrogen gas and placed under vacuum overnight. The protein film was stored at -20°C. Typical yield of the purified protein was 10 mg/L of M9 media. Labeling efficiency was ~94% as estimated by MALDI mass spectrometry (**Fig. S1d**). U-$^{13}$C-labeled ETM and U-$^{15}$N-labeled ETM were expressed and purified following the same protocol, but substituting $^{15}$N-$NH_4Cl$ or $^{13}$C-glucose with unlabeled reagents.

***Expression of 4-$^{19}$F-Phe fluorinated ETM***

A glycerol cell swab was used to start a 10 mL LB culture containing 50 µg/mL kanamycin. The starter culture was then used to inoculate 2 L of M9 media (pH 7.8, 48 mM $Na_2HPO_4$, 22 mM $KH_2PO_4$, 8.6 mM NaCl, 4 mM $MgSO_4$, 0.2 mM $CaCl_2$, 50 mg kanamycin) containing 3 g/L unlabeled glucose and 1 g/L unlabeled $NH_4Cl$. The cells were grown in M9 at 37°C for media for 8 hours until an $OD_{600}$ of 0.5. The cells were collected by centrifugation at 4,400x g for 10 min at 20°C, then concentrated into a fresh 1 L M9 culture and incubated at 30°C for 60 min. Subsequently, 1.5 g/L of glyphosate was added to halt the pentose phosphate pathway for aromatic amino acid synthesis [35], followed by addition of 115 mg L-Trp, 115 mg L-Tyr and 400 mg of 4-$^{19}$F-L-Phe to the culture. After 30 min, IPTG was added to a final concentration of 0.4 mM, and protein expression was allowed to proceed at 30°C for 5.5 hours. The cells were collected by centrifugation at 4,400x g for 10 min at 4°C. The pellet was stored at -70°C until purification. Cell lysis and protein purification followed the same protocol as outlined above, except that the ETM peak during preparative HPLC was collected in two fractions of approximately 1 min each. Fluorine incorporation in the two fractions was measured using MALDI mass spectrometry. The first fraction had a higher fluorine incorporation level of 83% for all three Phe residues labeled with $^{19}$F, indicating a per-residue labeling efficiency of 94% (**Fig. S1e**). Only this fraction was used to prepare the mixed $^{13}$C and $^{19}$F labeled protein for interhelical distance measurement. The final yield of the Phe-fluorinated ETM expression was 1.5 mg/L of M9 media. The protocol was originally tested using 100 mg/L of 4-$^{19}$F-Phe, 1.0 g/L of glyphosate, 6 g/L unlabeled glucose and with expression at 18°C for 5.5 hours, which yielded a much lower per-residue labeling efficiency of ~35%.

***Membrane sample preparation***

Eight proteins samples in two different lipid membranes were prepared for this study. Five membrane samples contained $^{13}$C, $^{15}$N-labeled ETM and one contained $^{13}$C-labeled ETM. Another sample contained a 1 : 1 mixture of $^{13}$C-labeled protein : $^{15}$N-labeled protein. The last sample contained a 1 : 1 mixture of $^{13}$C-labeled protein : 4-$^{19}$F-Phe-labeled protein. Six of the eight samples were prepared in a pH 7.5 Tris buffer (20 mM Tris-HCl, 5 mM NaCl, 2 mM ethylenediaminetetraacetic acid (EDTA) and 0.2 mM $NaN_3$). One sample was prepared in a pH 5 citrate buffer with calcium (20 mM Citrate, 5 mM $CaCl_2$ and 0.2 mM $NaN_3$), while the final sample was prepared in the same pH 5 citrate buffer without calcium chloride.

Chemical shift assignment and interhelical distance measurements were conducted on ETM bound to an ERGIC-mimetic membrane [36,37] containing 1-palmitoyl-2-oleoyl-glycero-3-phosphocholine (POPC), 1-palmitoyl-2-oleoyl-sn-glycero-3-phosphoethanolamine (POPE), bovine phosphatidylinositol (PI), 1-palmitoyl-2-oleoyl-sn-glycero-3-phospho-L-serine (POPS), and cholesterol (Chol). The POPC : POPE : PI : POPS : Chol molar ratios were 45 : 20 : 13 : 7 : 15. All lipids were purchased from Avanti Polar Lipids. The membrane has a protein : lipid molar ratio (P : L) of 1 : 20, and 2–4 mg $^{13}$C, $^{15}$N-labeled protein was used for most 2D and 3D correlation experiments. The intermolecular NHHC spectra were measured using a sample containing 4 mg each of $^{13}$C-labeled ETM and $^{15}$N-labeled ETM. This mixture was reconstituted into the ERGIC membrane at a P : L of 1 : 10 to increase the experimental sensitivity. $^{13}$C-$^{19}$F REDOR experiments

were conducted on 3.7 mg total of 1 : 1 mixed $^{13}$C-labeled and fluorinated ETM bound to the ERGIC membrane at P : L = 1 : 10.

To reconstitute ETM into lipid bilayers, we dissolved 2 mg protein in 1 mL trifluoroethanol (TFE) and mixed with appropriate amounts of lipids in 400 µL chloroform. For the HMA-bound sample, HMA was dissolved in TFE (1 mg/100 µL) and added to the protein-lipid mixture. The organic solvents were removed under a gentle stream of nitrogen gas, and the film was dried under vacuum at room temperature overnight. The proteoliposome film was resuspended in 3 mL of pH 7.5 sample buffer by vortexing and sonicating 2-3 times for 5 min until the suspension was homogenous. This was followed by 7 freeze-thaw cycles between a 42°C water bath and liquid nitrogen. The proteoliposomes were then pelleted using ultracentrifugation for 3 hours at 164,000x g and 4°C. The pellet was dried in a desiccator or under a gentle stream of nitrogen gas to a final hydration level of ~40% by mass and then packed into an appropriate MAS rotor using a benchtop centrifuge.

Drug binding to ETM was assessed in a "DMPX" membrane consisting of 1,2-dimyristoyl-sn-glycero-3-phosphocholine (DMPC) : 1,2-dimyristoyl-sn-glycero-3-phospho-(1'-rac-glycerol) (DMPG) at a 80% : 20% molar ratio. The mixture was chosen to maintain the same 20% anionic lipid fraction as the ERGIC membrane. A drug-free sample contained 2 mg of U-$^{13}$C, $^{15}$N-labeled ETM bound to the membrane at a P : L of 1 : 20. The sample containing 5-(N,N-hexamethylene)-amiloride (HMA) was prepared using a protein : drug (P : D) molar ratio of 1 : 1, with HMA (0.2 mg) added during organic solution mixing. The same P : L of 1:20 as the apo sample was used. After initial spectra showed only small CSPs, we titrated an additional 0.6 mg of HMA in 6 µl dimethyl sulfoxide (DMSO) into the proteoliposome, giving a P : D of 1 : 4. The solubility of HMA in aqueous solutions was very low (< 0.1 mg/ml), necessitating the use of DMSO. 3-$^{19}$F-amantadine (AMT) was titrated into the proteoliposome stepwise, from an initial P : D molar ratio of 1 : 1 to a final P : D of 1 : 8. The protein/lipid molar ratio of the sample is 1 : 15. The fluorinated AMT has high solubility in water, thus can be mixed with the membrane directly. For the $^{13}$C-$^{19}$F REDOR experiments, the sample was packed in a 1.9 mm MAS rotor, while chemical shift measurements were conducted in a 3.2 mm MAS rotor on the 800 MHz spectrometer.

Chemical shift changes under acidic pH and with added calcium were assessed in the same "DMPX" membrane. The sample with 5 mM $CaCl_2$ at pH 5 contained 2 mg of U-$^{13}$C, $^{15}$N-labeled ETM bound to the membrane at a P : L of 1 : 20, while the sample without calcium contained 2 mg of U-$^{13}$C-labeled ETM bound to the membrane at a P : L of 1 : 20.

**Synthesis of F-Amt**

The synthetic protocol (Scheme S1) used for preparation of F-Amt was adapted from that described by Jasys and coworkers (Jasys, V. J.; Lombardo, F.; Appleton, T. A.; Bordner, J.; Ziliox, M.; Volkmann, R. A. Preparation of Fluoroadamantane Acids and Amines: Impact of Bridgehead Fluorine Substitution on the Solution-and Solid-State Properties of Functionalized Adamantanes. *J. Am. Chem. Soc.* **2000**, *122*, 466-473). Thus, the reaction between 1-adamantanecarboxylic acid and $KMnO_4$ afforded 3-hydroxyadamantanecarboxylic acid which was transformed through its tetrabutylammonium salt to the corresponding methyl ester. The fluorination of the hydroxyester was accomplished through treatment with diethylaminosulfur trifluoride (DAST) at -50 °C. The 3-fluoroadamantane-1-amine acetate (F-Amt acetate) was obtained by treatment of 3-fluoroadamantanecarboxylic acid with diphenylphosphorylazide (DPPA) and subsequent hydrogenolysis of the resultant benzyl carbamate.

Scheme S1

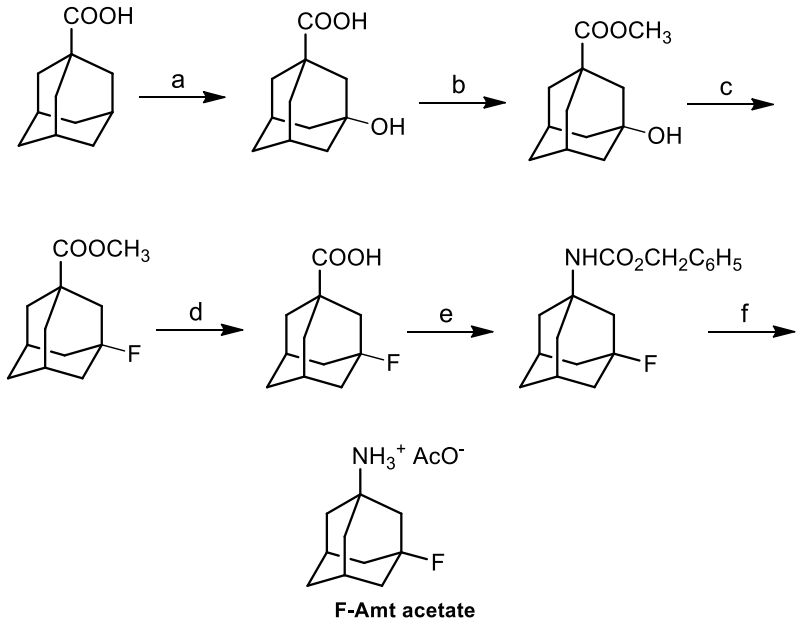


**F-Amt acetate**

Reagents and Conditions: (a) $KMnO_4$, KOH, 50 °C; (b) $TBAHSO_4$, $NaHCO_3$, $CH_3I$, acetone, 48 h, r.t.; (c) DAST, $CH_2Cl_2$, 3 h, -50 °C → 60 °C; (d) NaOH, MeOH, THF, $H_2O$, 24 h, r.t.; (e) DPPA, TEA, BnOH, benzene, 70 °C; (f) $H_2$, 10 % Pd/C, AcOH.

3-fluoroadamantane-1-amine acetate (F-Amt acetate): $^1$H-NMR (phosphate buffer, pH 7, 10 % $D_2O$, 500 MHz) $\delta$ (ppm) 1.60-1.69 (m, 2H, 6-H), 1.87 (s, 4H, 4,10-H), 1.89-1.98 (m, 7H, 8,9-H, $CH_3COO^-$), 2.09 (br d, 2H, 2-H), 2.48 (br s, 2H, 5,7-H); LC-MS (m/z) 170.3 ($FC_{10}H_{14}NH_3^+$). *Base:* mp 210 °C (EtOH-ether); $^1$H-NMR ($CDCl_3$, 400 MHz) $\delta$ (ppm) 1.41 (br s, 2H, 6-H), 1.49 (br s, 2H, $NH_2$), 1.51 (br s, 4H, 4,10-H), 1.74 (br d, 2H, $J$ = 5.8 Hz, 2-H), 1.79 (br m, 4H, 8,9-H), 2.31 (br s, 2H, 5,7-H); $^{13}$C-NMR ($CDCl_3$, 50 MHz) $\delta$ (ppm) 31.33, 31.55 (5,7-C), 34.67 (6-C), 41.44, 41.77 (4,10-C), 44.74 (8,9-C), 51.14, 51.47 (2-C, 3-C), 93.29 (d, $J_{C\text{-}F}$ = 183.8 Hz, 1-C). Anal. Acetate ($C_{12}H_{20}NO_2F$) (EtOH-$Et_2O$). Calc. C: 62.86 H: 8.79. Found. C: 62.56 H: 8.99.

***Solid-state NMR experiments***

Most solid-state NMR spectra were measured on a Bruker AVANCE NEO 900 MHz (21.1 T) spectrometer and an Avance II 800 MHz (18.8 T) spectrometer using 3.2 mm HCN probes. Intermolecular $^{13}$C-$^{19}$F REDOR experiments were conducted on an Avance III HD 600 MHz (14.1 T) spectrometer using a 1.9 mm HFX probe. MAS frequencies were 11.8 kHz for all 900 MHz experiments and 14 kHz for the 800 and 600 MHz experiments. Radiofrequency (RF) field strengths on the 3.2 mm probes were 50-91 kHz for $^1$H, 50-63 kHz for $^{13}$C, and 33-42 kHz for $^{15}$N. RF field strengths on the 1.9 mm MAS probe were 83-130 kHz for $^1$H, 62.5 kHz for $^{13}$C, and 71 kHz for $^{19}$F. Sample temperatures are direct readings from the probe thermocouple, whereas actual sample temperatures are 5-15 K higher at the MAS frequencies employed. $^{13}$C chemical shifts are reported on the tetramethylsilane scale using the adamantane $CH_2$ chemical shift at 38.48 ppm as an external standard. $^{15}$N chemical shifts are reported on the liquid ammonia scale using the N-acetylvaline peak at 122.00 ppm as an external standard.

2D $^{13}$C-$^{13}$C correlation experiments were conducted using COmbined -Driven (CORD) mixing [38] for $^{13}$C spin diffusion. 2D and 3D $^{15}$N-$^{13}$C correlation spectra, namely, NCACX, NCOCX, and CONCA [39], were measured on the 900 MHz spectrometer. These experiments used SPECtrally Induced Filtering In Combination with Cross Polarization (SPECIFIC-CP) [40] for heteronuclear

polarization transfer. Water-edited 2D $^{15}$N-$^{13}$Cα correlation spectra were measured under 11.8 kHz MAS [19,20] using $^{1}$H mixing times of 9 ms and 100 ms. 2D $^{15}$N-$^{13}$C correlation spectra were measured using an out-and-back Transferred-Echo Double Resonance (TEDOR) pulse sequence on the 800 MHz NMR [41]. Intermolecular 2D NHHC correlation spectra [42] were measured used 0.5 ms and 1 ms $^{1}$H-$^{1}$H mixing. 1D and 2D $^{13}$C-$^{19}$F REDOR experiments [18,43,44] were conducted to measure distances between 4-$^{19}$F-Phe-labeled and $^{13}$C-labeled ETM, and to measure dipolar dephasing of $^{13}$C-labeled ETM by 3-$^{19}$F-AMT. Additional specific parameters for the NMR experiments are given in **Table S5**.

***NMR spectral analysis***

NMR spectra were processed in the TopSpin software while chemical shifts were assigned in Sparky [45]. TALOS-N [46] was used to calculate (ϕ, ψ) torsion angles after converting the $^{13}$C chemical shifts to the DSS scale. Residue-specific chemical shift differences between drug bound and apo samples were calculated from the measured $^{13}$C and $^{15}$N chemical shifts according to:

$$\Delta\delta = \sqrt{\left[\sum_{C_i}\left(\delta_{C_i}^{drug} - \delta_{C_i}^{apo}\right)^2 + \frac{\left(\delta_N^{drug} - \delta_N^{apo}\right)^2}{2.5}\right]} \quad (1)$$

2D heatmaps of normalized water-edited 2D NCA spectra were generated using an in-house Python script that removes spectral noise while calculating intensity ratios. The intensities of the 9 ms and 100 ms spin diffusion spectra of the ERGIC-bound ETM were read using the NMRglue package [47]. Spectral intensity was noise filtered by setting signal lower than 3.5 times the average noise level in an empty region of the 2D spectrum to zero for the S spectrum and to a large number for the $S_0$ spectrum [28,48]. The intensities were divided and scaled by the number of scans to obtain a 2D contour map, $I_{9\ ms}/I_{100\ ms}$.

The water accessibility data for the closed high-pH state of influenza BM2 proton channel (**Fig. 2f**) for comparison with the ETM data were originally measured in 2D $^{13}$C-$^{13}$C correlation spectra with 4 ms (S) and 100 ms ($S_0$) $^{1}$H-$^{1}$H spin diffusion [28]. To enable comparison with the ETM water-edited spectra measured at 9 ms and 100 ms $^{1}$H mixing, we scaled the BM2 S (4 ms) /$S_0$ (100 ms) ratios by the integrated aliphatic intensity ratio of 1.976 between the 1D BM2 water-edited spectra with 9 ms and 4 ms $^{1}$H mixing. This scaling factor was verified to be accurate for two resolved sites, T24 and G26, in the 1D $^{13}$C spectra of BM2.

***Simulation of the $^{13}$C-$^{19}$F REDOR curves***

$^{13}$C-$^{19}$F REDOR data were simulated using the SIMPSON software [49]. The simulations accounted for finite $^{19}$F and $^{13}$C 180° pulse lengths and $^{19}$F pulse imperfections by co-adding REDOR curves for $^{19}$F flip angles of 180° to 145° using a normal distribution centered at 180° with a standard deviation of 15° [43]. The simulations also included $^{19}$F chemical shift anisotropy (CSA), which was obtained from the $^{19}$F CSA sideband patterns measured at 293 K under 14 kHz MAS. The sideband intensities were fit using the Solids Lineshape Analysis module in Topspin. The best-fit CSA was $\delta_{CSA}$ = 55±2 ppm and η = 0.6±0.1 for the $^{19}$F peak at $\delta_{iso}$ = -113.5 ppm and $\delta_{CSA}$ = 53±2 ppm and η = 0.5±0.1 for the $^{19}$F peak at $\delta_{iso}$ = -117.5 ppm. These CSAs indicate that all three 4-$^{19}$F-Phe residues are immobilized.

REDOR distance analysis required two other considerations. First, the 1 : 1 $^{13}$C and $^{19}$F mixed peptides means that only 50% of all $^{13}$C-labeled helices have an adjacent $^{19}$F-labeled helix. Thus, the lowest possible REDOR S/$S_0$ value is 0.5. Second, while most $^{13}$C-$^{19}$F REDOR restraints came from 2D $^{13}$C-$^{13}$C resolved peaks, dephasing to sidechain carbons were obtained from 1D

$^{13}$C spectra with resonance overlap. These overlapped peaks will not experience complete dipolar dephasing if some of the carbons contributing to an overlapped signal are far from a fluorine. We first identified the residues experiencing dephasing by $^{19}$F from the 2D $^{13}$C-$^{13}$C correlation spectra. These peaks then guided the assignment of the 1D $^{13}$C-$^{19}$F spectra. For example, both A22 and A32 Cβ resonate at 16.6 ppm, but only A22 Cα is dephased in the 2D $^{13}$C-$^{13}$C spectrum (**Fig. 2b**). Thus, we assigned the 16.6 ppm dephased signal in the 1D $^{13}$C-$^{19}$F REDOR spectra to A22 Cβ. Making the reasonable assumption that each Ala Cβ contributes equal intensity, we account for this overlap factor by correcting the experimental dephasing $(S/S_0)_{exp}$ values according to:

$$\left(S/S_0\right)_{adj} = 1 - \left[2 \times \left(1 - \left(S/S_0\right)_{exp}\right) \times f\right] \quad (2)$$

where *f* is the fraction of an overlapped $^{13}$C peak that is dephased by $^{19}$F. For example, for the 2-fold overlapped 16.6-ppm Ala Cβ peak with *f* = 2, the lowest possible $(S/S_0)_{exp}$ value is ~0.75, which gives a minimal $(S/S_0)_{adj}$ of ~0.0.

The random uncertainty $\sigma(S/S_0)_{exp}$ of the measured $(S/S_0)_{exp}$ values were propagated from the signal-to-noise ratios (SNRs) of the REDOR $S_0$ and S spectra. The upper and lower limits for the $(S/S_0)_{adj}$ values were obtained by adding or subtracting the $\sigma(S/S_0)_{exp}$ to the $(S/S_0)_{exp}$ values before using equation (2), respectively. Best-fit distances were obtained as the distance with the lowest $\chi^2$ value between the $(S/S_0)_{adj}$ values and simulated $S/S_0$ intensities. Upper and lower distance limits were specified using the upper and lower limits for the $(S/S_0)_{adj}$ values calculated as described above. For an upper limit of $(S/S_0)_{adj}$ >0.95 indicating a negative contact (i.e. dephasing was not significant), an upper limit of 50 Å was used. The final lower and upper distance limits for structure calculation were set by multiplying the uncertainty obtained in this manner by 2 times or by choosing distances that are 2.0 Å from the best-fit value, whichever was larger, to loosen the constraints.

***XPLOR-NIH structure calculations and analysis***

Initial structure calculation attempts using ambiguous interhelical contacts, where a central helix can contact both neighboring helices, did not converge. Thus, we generated parallel pentameric models (**Fig. S7**) to specify the $^{13}$C-$^{19}$F and NHHC intermolecular distance restraints in a directional fashion where possible. The models take into account the water- and lipid-edited spectra (*vide infra*) to pinpoint the pore-facing versus lipid-facing orientation of the residues. An ideal helix model that puts N15, L19, V25, L31 and T35 to be pore-facing and Phe sidechains to be lipid-facing does not satisfy all the experimental constraints (**Fig. S7a**). The measured Cβ secondary shifts (**Fig. S3b**), with L21 having a 1.4 ppm downfield-shifted Cβ compared to the average of all other helical Leu residues, indicate that the helix is disordered between residues F20 and F23, consistent with previous solution NMR data [10]. Given this disorder, we generated four alternative models (**Fig. S7b-e**) that satisfy the measured interhelical Phe-Phe $^{13}$C-$^{19}$F contacts. Only one model with F26-F23 interhelical contact adequately reproduces the key features of the experimental data. This model was then used to disambiguate the NHHC and $^{13}$C-$^{19}$F distance restraints (**Tables S2, S3**), by mainly considering only residues that are less than four residues away in the primary sequence and that are in close proximity between two helical wheels. With this approach, 42 of the 87 interhelical restraints were set to be unambiguous.

We calculated the ETM structure for residues 8-38 using XPLOR-NIH [50] hosted on the NMRbox computing platform [51]. The calculation contained two stages. In the first, annealing, stage, five extended ETM monomers were placed in a parallel pentamer geometry with each monomer located 20 Å from the center of the pentamer. A total of 120 independent XPLOR-NIH runs were performed with 5,000 steps of torsion angle dynamics at 5,000 K followed by annealing to 20 K

in decrements of 20 K with 100 steps at each temperature. After the annealing, final energy minimizations in torsion angle and Cartesian coordinates were carried out. The five monomers were restrained to be identical in the annealing step using the non-crystallographic symmetry term PosDiffPot and the translational symmetry term DistSymmPot. Chemical-shift derived (ϕ, ψ) torsion angles predicted by TALOS-N were implemented with the XPLOR dihedral angle restraint term CDIH with ranges set to the higher value between twice the TALOS-N predicted uncertainty and 20°. The interhelical distance restraints (**Tables S2, S3**) were implemented using the NOE potential. Distance upper limits were set to 9.0 Å and 11.5 Å for 500 μs and 1000 μs of $^{1}$H-$^{1}$H mixing for the NHHC constraints. Negative REDOR contacts, i.e., $^{13}$C sites without dephasing, were implemented as two NOE's: one to each neighboring helix. Implicit hydrogen bonds using the hydrogen-bonding database potential term HBDB were implemented during annealing to favor formation of the α-helix conformation. Finally, standard XPLOR potentials were used to restrain the torsion angles using a structural database with the term TorsionDB, and standard bond angles and lengths were set with terms BOND, ANGL, IMPR and RepelPot. The structures were sorted by energy, using all the potentials in the calculation. The scales for all potentials are given in **Table S4**.

In the second, structure refinement, stage, the three lowest-energy structures from the annealing stage were used as independent inputs. A total of 64 independent XPLOR-NIH runs from each of the three starting structures were performed with 5,000 steps of torsion angle dynamics at 1,000 K followed by annealing to 20 K in decrements of 10 K with 100 steps at each temperature. This was followed by final energy minimizations in torsion angle and Cartesian coordinates. All the potentials employed in annealing were also used during refinement, with two additions. The $^{13}$C-$^{13}$C correlations were implemented as intramolecular NOE distance restraints with an upper limit of 8.0 Å. Inter-residue cross peaks to long hydrophobic side chains such as Phe, Ile, and Leu were sometimes violated, and consequently the upper limits for these 5% of restraints were increased to 12.0 Å. Explicit hydrogen bonds for residues I13 (hydrogen-bonded to V17) – N15 (hydrogen-bonded to L19) and F23 (hydrogen-bonded to L27) – T30 (hydrogen-bonded to L34) were substituted for implicit hydrogen bonds, using the same HBDB potential. Finally, the scales of the NOE, Repel, and TorsionDB potentials were increased (**Table S4**). All 192 structures from the three independent runs were pooled and sorted using the CDIH, NOE, HBDB, BOND, ANGL, IMPR, Repel and Repel14 potentials, while excluding PosDiffPot, DistSymmPot and TorsionDB potentials. The ten structures with the lowest energies across the specified potentials were included in the final structural ensemble.

Graphical images depicting the structures were generated in PyMOL v2.3.4. The reported channel radii were calculated using the HOLE program [52], and represent the radii of the largest sphere that can be accommodated from exclusion of the van der Waals diameter of all atoms at each XY plane along the Z channel coordinate, which is collinear with the bilayer normal and the putative direction of ion permeation. The cutoff radius for the calculation was set to be 5 Å. The output from HOLE was visualized in PyMOL by setting the van der Waals radius of the HOLE-generated spheres 'SPH' to the b-factor values of the SPH output by HOLE.

***Docking of HMA to ETM structure***

The coordinate file for HMA was generated from bond connectivity using the Chem3D module of ChemDraw Professional 18.1. Ligand geometry was optimized within Chem3D using the MM2 energy minimization module. Docking was performed using the HADDOCK 2.4 webserver using the ensemble of the ten lowest-energy protein structures calculated in XPLOR-NIH. The docking was constrained only with an active list. Active residues were defined as the N-terminal residues with significant CSPs (**Fig. 4c)**:T9, G10, T11, I13, and S16. Several docking runs were conducted using constraints to this list of residues on all helices, one of the five helices, and different

combinations of two of the five helices. Docking calculations were performed using default settings in the HADDOCK 2.4 webserver interface, except that the solvent for the final structural refinement were varied as DMSO and water. The N- and C-termini were set as uncharged as the structural model does not include the full protein sequence. Passive residues were automatically defined around the active residues with a 6.5 Å surface radius cutoff. Non-polar hydrogens were removed from the calculation, and 2 partitions for random exclusion of Ambiguous Interaction Restraints ('AIRs') were used (50% of AIRs were randomly excluded in the calculation). The docking used 1000 structures for rigid-body docking with 5 trials of rigid-body minimization. Semi-flexible refinement was done with 200 structures selected from the rigid-body minimization stage. Final refinement with explicit solvent (DMSO or water) were performed on all 200 structures from semi-flexible refinement. Output structures were aligned and analyzed in Pymol 2.3.5.

In docking with DMSO as a refinement solvent, 200 refined structures were grouped into 5 clusters, with 154 structures belonging to the lowest energy cluster 1. The four best structures of this cluster had an average HADDOCK score of -29.8 +/- 2.1, and a Z-score of -1.7. Similar results were obtained with docking with water as a refinement solvent, the 200 refined structures were grouped into three clusters, where cluster 1 contained 170 structures. The four best structures this cluster had a HADDOCK score of -29.3 +/- 1.9, with a Z-score of -1.4.

The majority of docked structures converged to a state where HMA partitioned to the N-terminal entry cavity of the channel, but the HMA orientation is variable. Visual inspection showed three distinct orientations: 1) HMA tilted and diving into the pore with the hexamethylene ring facing up (**Fig. S9a**), 2) HMA tilted and diving into the pore with the ring facing down (**Fig. S9b**), 3) HMA laying horizontally across the top of the channel, with the guanidinium intercalated between two helices (**Fig S9c**). Among the 32 lowest energy structures in the DMSO and water docking results, 13/32 structures belonged to the first mode (ring up), 6/32 to the second mode (ring down), and 13/32 to the third mode (horizontal). All these modes indicate a pore-occlusion mechanism, similar to the amantadine inhibition mechanism of the influenza AM2 proton channel [9].

Given the hydrophobic nature of HMA, another possible binding mode would be drug binding from the lipid side to the exterior of the helical bundle. This mode could explain the chemical shift perturbation of the lipid-facing S16, but the mechanism of inhibition would be indirect allosteric narrowing of the pore, and would require multiple drug molecules to bind each pentamer to preserve the symmetry, as only a single set of peaks are observed in the drug-bound protein spectra. Thus we consider this mechanism less likely than direct occlusion of the pore. The lipid-binding mode was only observed in docking runs with only one or two helices containing the active residues.

## Method References


35 Lehninger, A. L., Nelson, D. L. & Cox, M. M. *Principles of Biochemistry*. 2nd edn, (Worth Publishers, 1993).

36 Casares, D., Escribá, P. V. & Rosselló, C. A. Membrane Lipid Composition: Effect on Membrane and Organelle Structure, Function and Compartmentalization and Therapeutic Avenues. *Int. J. Mol. Sci.* **20**, (2019).

37 van Meer, G., Voelker, D. R. & Feigenson, G. W. Membrane lipids: where they are and how they behave. *Nat. Rev. Mol. Cell Biol.* **9**, 112-124, (2008).

38 Hou, G., Yan, S., Trebosc, J., Amoureux, J. P. & Polenova, T. Broadband homonuclear correlation spectroscopy driven by combined R2(n)(v) sequences under fast magic angle

spinning for NMR structural analysis of organic and biological solids. *J. Magn. Reson.* **232**, 18-30, (2013).
39 Rienstra, C. M., Hohwy, M., Hong, M. & Griffin, R. G. 2D and 3D 15N-13C-13C NMR chemical shift correlation spectroscopy of solids: assignment of MAS spectra of peptides. *J. Am. Chem. Soc.* **122**, 10979-10990, (2000).
40 Baldus, M., Petkova, A. T., Herzfeld, J. & Griffin, R. G. Cross polarization in the tilted frame: assignment and spectral simplification in heteronuclear spin systems. *Mol. Phys.* **95**, 1197-1207, (1998).
41 Hong, M. & Griffin, R. G. Resonance Assignment for Solid Peptides by Dipolar-Mediated 13C/15N Correlation Solid-State NMR. *J. Am. Chem. Soc.* **120**, 7113-7114, (1998).
42 Lange, A., Luca, S. & Baldus, M. Structural constraints from proton-mediated rare-spin correlation spectroscopy in rotating solids. *J. Am. Chem. Soc.* **124**, 9704-9705, (2002).
43 Shcherbakov, A. A. & Hong, M. Rapid measurement of long-range distances in proteins by multidimensional (13)C-(19)F REDOR NMR under fast magic-angle spinning. *J. Biomol. NMR* **71**, 31-43, (2018).
44 Shcherbakov, A. A., Roos, M., Kwon, B. & Hong, M. Two-dimensional 19F-13C correlation NMR for 19F resonance assignment of fluorinated proteins. *J. Biomol. NMR* **74**, 193-204, (2020).
45 Lee, W., Tonelli, M. & Markley, J. L. NMRFAM-SPARKY: enhanced software for biomolecular NMR spectroscopy. *Bioinformatics* **31**, 1325-1327, (2014).
46 Shen, Y. & Bax, A. Protein backbone and sidechain torsion angles predicted from NMR chemical shifts using artificial neural networks. *J. Biomol. NMR* **56**, 227-241, (2013).
47 Helmus, J. J. & Jaroniec, C. P. Nmrglue: an open source Python package for the analysis of multidimensional NMR data. *J. Biomol. NMR* **55**, 355-367, (2013).
48 Dregni, A. J., Duan, P. & Hong, M. Hydration and Dynamics of Full-Length Tau Amyloid Fibrils Investigated by Solid-State Nuclear Magnetic Resonance. *Biochemistry* **59**, 2237-2248, (2020).
49 Bak, M., Rasmussen, T. & Nielsen, N. C. SIMPSON: A General Simulation Program for Solid-State NMR Spectroscopy. *J. Magn. Reson.* **147**, 296-330, (2000).
50 Schwieters, C. D., Kuszewski, J. J., Tjandra, N. & Clore, G. M. The Xplor-NIH NMR molecular structure determination package. *J. Magn. Reson.* **160**, 65-73, (2003).
51 Maciejewski, M. W. *et al.* NMRbox: A Resource for Biomolecular NMR Computation. *Biophys. J.* **112**, 1529-1534, (2017).
52 Smart, O. S., Neduvelil, J. G., Wang, X., Wallace, B. A. & Sansom, M. S. HOLE: a program for the analysis of the pore dimensions of ion channel structural models. *J. Mol. Graph* **14**, 354-360, 376, (1996).

**Acknowledgements**
This research is funded by National Institutes of Health grant GM088204 to M.H and the MIT School of Science Sloan Fund to V.S.M. and A.A.S. The experiments made use of NMR spectrometers at the MIT/Harvard Center for Magnetic Resonance, supported by NIH grant P41 GM132079. Structure calculation made use of the NMRbox, supported by NIH grant P41 GM111135.

**Author contributions**
V.S.M., M.J.M. and A.A.S. cloned, expressed and purified the protein and conducted the solid-state NMR experiments. V.S.M and M.J.M. assigned and analyzed the spectra. V.S.M calculated the structure with contributions from A.J.D. and M.J.M. A.A.S. conducted $^{19}F$ NMR experiments, simulations and docking. A.K. provided fluorinated amantadine. M.H. designed the project and supervised data analysis. All authors discussed the results of the study and wrote the paper.

**Competing interests**
The authors declare no competing financial interests.

**Corresponding author:**
Correspondence and requests for information about the data shown here should be addressed to Mei Hong, meihong@mit.edu.

**Data availability**
NMR chemical shifts, distances and torsion-angle restraints have been deposited in the Biological Magnetic Resonance Bank (BMRB) with ID numbers 30795. The structural coordinates for ETM have been deposited in the Protein Data Bank with accession codes 7K3G.

# Extended Data Figures and Tables

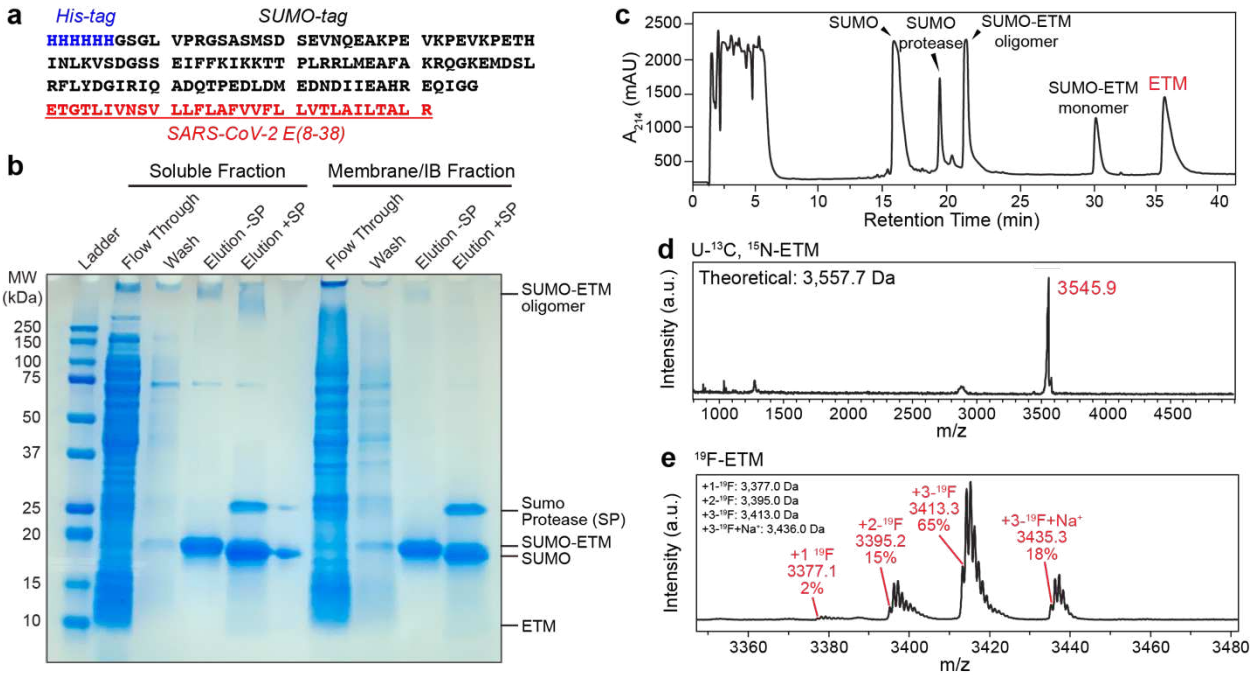


**Figure S1**. Cloning, purification and characterization of SARS-CoV-2 ETM. (**a**) SUMO-tagged ETM sequence. (**b**) SDS-PAGE gel showing purification of ETM by $Ni^{2+}$-affinity column chromatography. The flowthrough contains all soluble proteins that have low affinity for $Ni^{2+}$. The column was washed with 30 mM imidazole, and SUMO-ETM (18 kDa band) was eluted at >90% purity with 250 mM imidazole. High molecular-weight SUMO-ETM oligomers are visible as a minor species. ETM was cleaved from the SUMO fusion tag using SUMO protease (SP). (**c**) Preparative reverse-phase HPLC chromatogram after protease cleavage. ETM elutes at 37.5 min. (**d**) MALDI mass spectrum of purified U-$^{13}$C, $^{15}$N labeled ETM. (**e**) MALDI mass spectrum of purified 4-$^{19}$F-Phe labeled ETM. The measured masses show excellent agreement with the theoretical masses. 83% of the 4-$^{19}$F-Phe labeled ETM monomers have all three Phe residues fluorinated, indicating a per-site labeling efficiency of 94%.

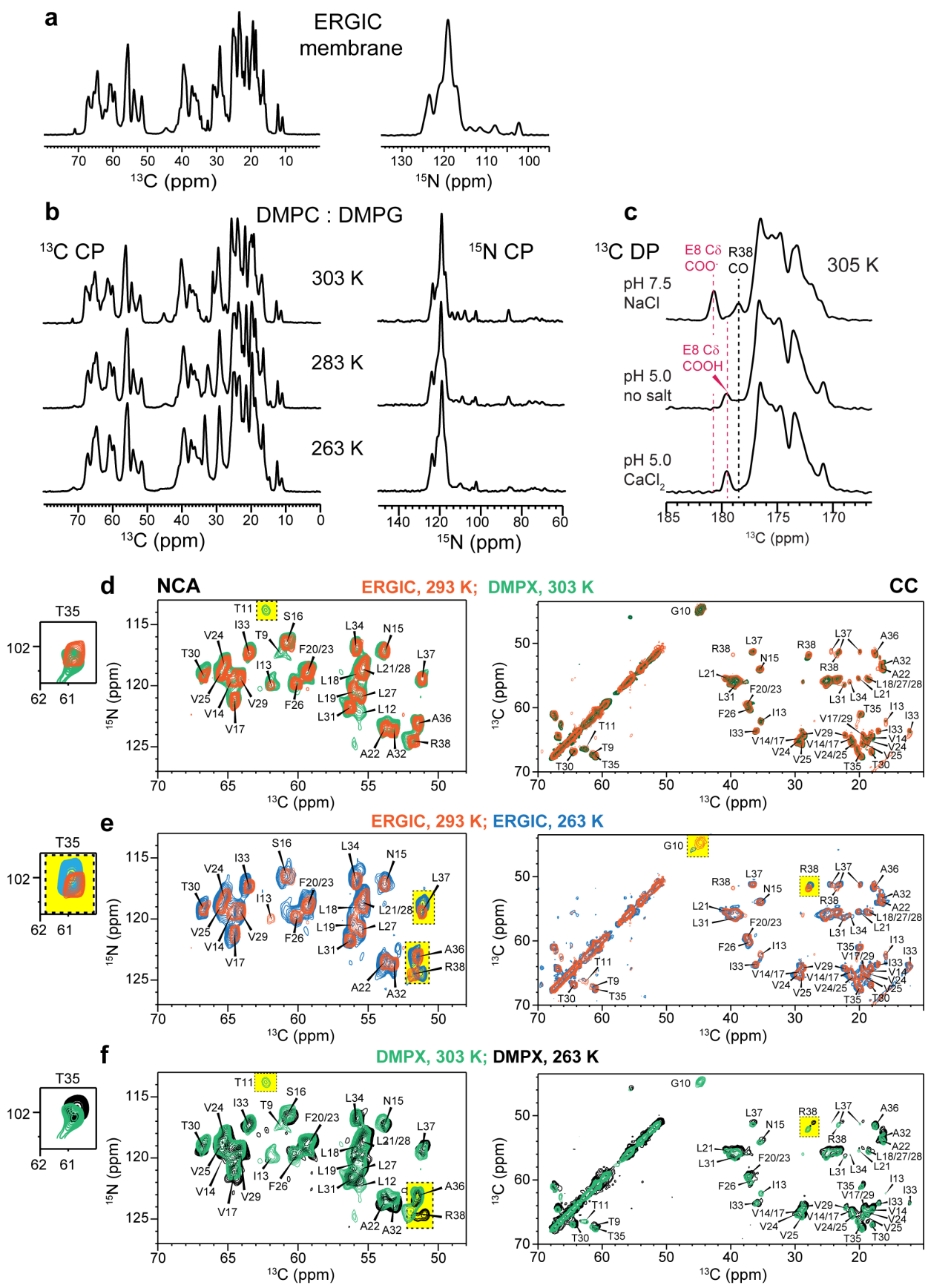
a
ERGIC
membrane
70 60 50 40 30 20 10
13C (ppm)
130 120 110 100
15N (ppm)
b
DMPC : DMPG
13C CP
303 K
283 K
263 K
70 60 50 40 30 20 10 0
13C (ppm)
15N CP
140 120 100 80 60
15N (ppm)
c
13C DP
E8 Cδ COO-
R38 CO
305 K
pH 7.5
NaCl
E8 Cδ COOH
pH 5.0
no salt
pH 5.0
CaCl2
185 180 175 170
13C (ppm)
d
NCA
ERGIC, 293 K; DMPX, 303 K
CC
T35
102
62 61
115 120 125
15N (ppm)
70 65 60 55 50
13C (ppm)
T11 S16 I33 V24 T9 T30 F20/23 I13 L34 N15 L37 L21/28 L18 L27 L19 L12 L31 V25 V14 V29 F26 V17 A36 R38 A22 A32
50 60 70
13C (ppm)
40 30 20
13C (ppm)
G10 R38 L37 N15 L21 L31 F20/23 F26 I13 I33 V14/17 V24 V25 T11 T9 T30 T35 A36 A32 A22 L18/27/28 L34 V17/29 V29 V14 V24/25 T30
e
ERGIC, 293 K; ERGIC, 263 K
f
DMPX, 303 K; DMPX, 263 K

**Figure S2**. Effects of temperature and membrane composition on ETM structure. (**a**) 1D $^{13}C$ and $^{15}N$ CP-MAS spectra of ERGIC membrane-bound ETM. The spectra show high sensitivity and resolution, indicating a well ordered and rigid structure. (**b**) 1D $^{13}C$ and $^{15}N$ CP-MAS spectra of ETM in DMPC : DMPG membranes from 303 K to 263 K. The spectral intensities and linewidths are insensitive to temperature, indicating that the protein is mostly immobilized at ambient temperature. (**c**) $^{13}C$ direct-polarization (DP) spectra of DMPX-bound ETM, showing the Glu8 sidechain carboxyl chemical shift change between high and low pH, indicating the protonation of this N-terminal residue at low pH. (**d-f**) 2D $^{15}N$-$^{13}C$ (left) and $^{13}C$-$^{13}C$ (right) correlation spectra of ETM at high and low temperatures and in different membranes. Yellow shaded areas highlight peaks with significant chemical shift or intensity changes. (**d**) 2D correlation spectra of ERGIC-bound ETM (*orange*) at 293 K and DMPC : DMPG bound ETM at 303 K (*green*). The chemical shifts are similar, indicating that the protein conformation is mostly unaffected by the presence of POPS, POPI and cholesterol. The T11 signal is not detected in the ERGIC membrane. (**e**) 2D correlation spectra of ERGIC-bound ETM at 293 K (*orange*) and 263 K (*blue*). Moderate chemical shift changes are observed for C-terminal residues from T35 to R38. (**f**) 2D correlation spectra of DMPC : DMPG-bound ETM at 303 K (*green*) and 263 K (*purple*). The C-terminal residues exhibit temperature-dependent chemical shifts that are similar to the ERGIC-bound peptide. The N-terminal residues of T9 to I13 do not show signals at 263 K, indicating that the N-terminus undergoes intermediate-timescale motion at low temperature. Thus, the ETM C-terminal conformation is temperature-dependent while the N-terminus is dynamic at high temperature.

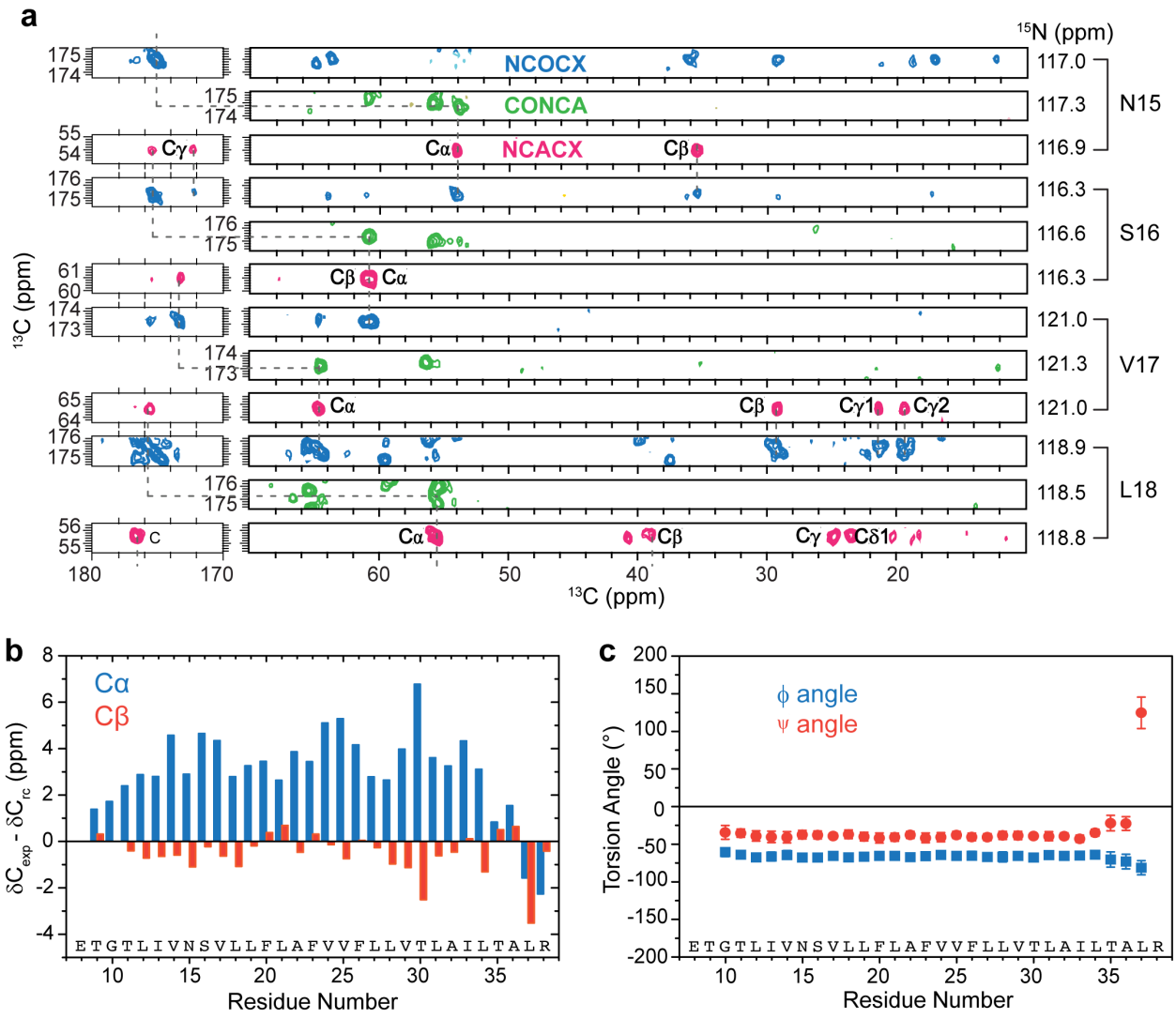


**Figure S3**. Chemical shift assignment and secondary structure of ETM. (**a**) Representative strips from 3D NCACX (*magenta*), CONCA (*green*) and NCOCX (*blue*) spectra of ERGIC-membrane bound ETM. These 3D spectra allow full assignment of the $^{13}C$ and $^{15}N$ chemical shifts. (**b**) Cα (*blue*) and Cβ (*orange*) secondary chemical shifts compared to the random coil chemical shifts. Most residues show positive Cα and negative Cβ secondary shifts, indicating an α-helical secondary structure. (**c**) (φ, ψ) torsion angles calculated using TALOS-N. Residues G10 to L34 show α-helical conformation.

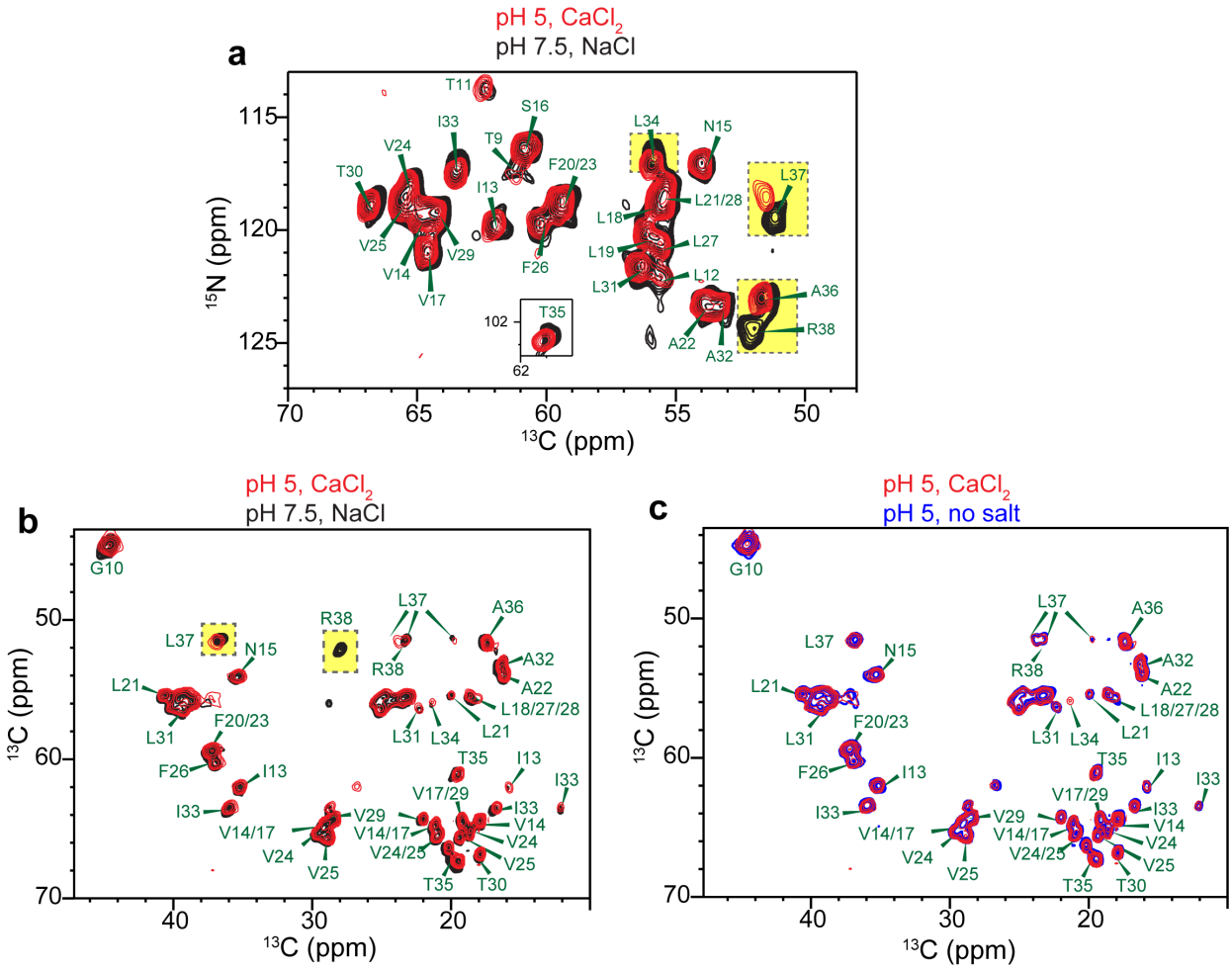


**Figure S4**. Effects of pH and ions on the chemical shifts of ERGIC-membrane bound ETM. Where cations are present, the ion concentration is 5 mM. (**a**) 2D $^{15}$N-$^{13}$Cα correlation spectra of high-pH ETM with 5 mM NaCl and low-pH ETM with 5 mM $CaCl_2$. Chemical shift changes are observed for C-terminal residues such as R38, L37 and L34 (yellow highlighted regions). (**b**) 2D $^{13}$C-$^{13}$C correlation spectra of low-pH ETM with $CaCl_2$ and high-pH ETM with NaCl. (**c**) 2D $^{13}$C-$^{13}$C correlation spectrum of low-pH ETM with $CaCl_2$ and low-pH ETM without salt. These spectra show that chemical shift changes mainly result from pH changes.

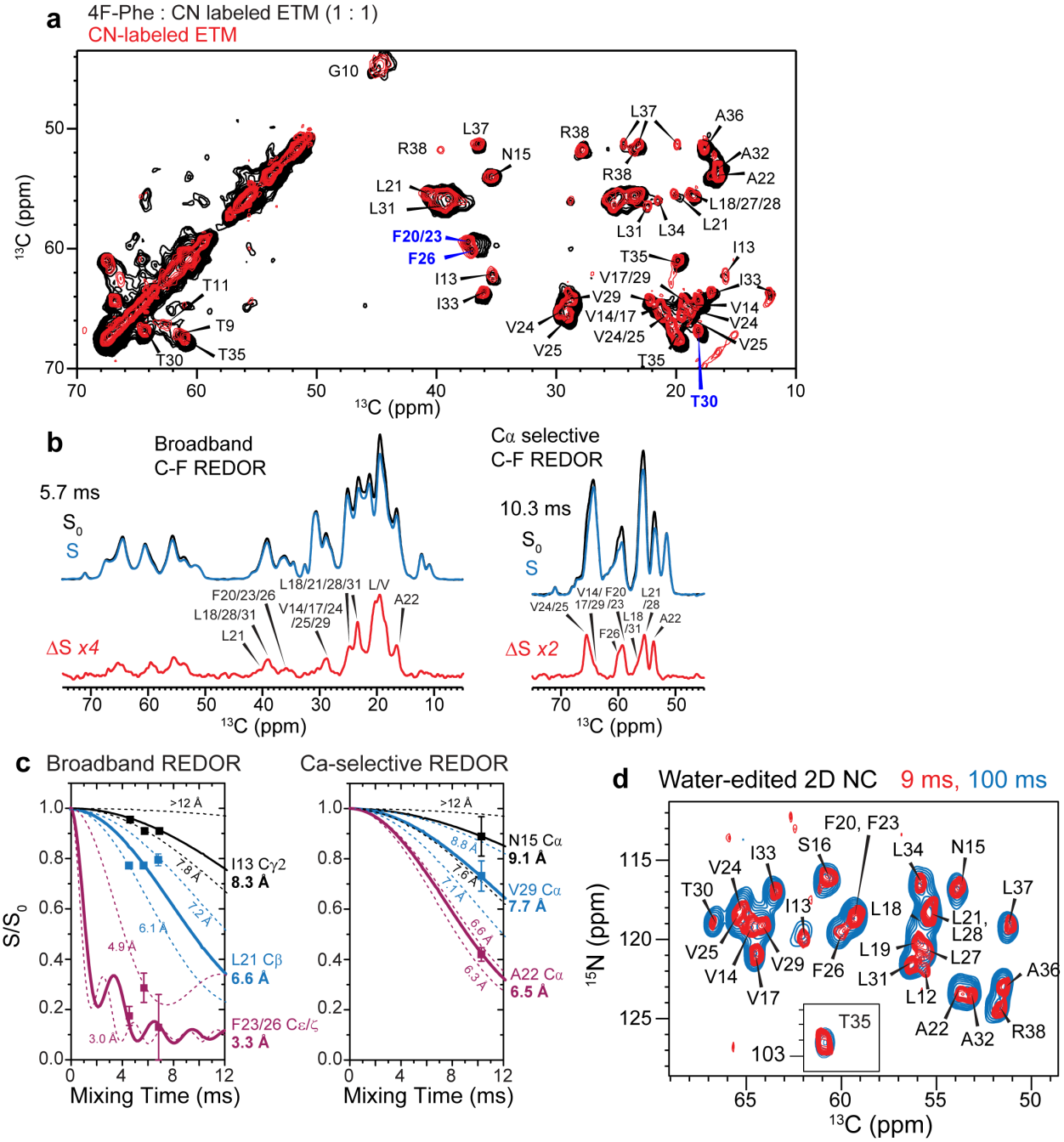


**Figure S5**. Additional $^{13}C$-$^{19}F$ REDOR spectra and water-edited spectra to determine the interhelical assembly of ETM. (**a**) 2D $^{13}C$-$^{13}C$ correlation spectrum of mixed 4-$^{19}F$-Phe labeled and U-$^{13}C$,$^{15}N$-labeled ETM (*black*). The $^{13}C$ chemical shifts of most residues are similar to the $^{13}C$,$^{15}N$-labeled protein (*red*), indicating that fluorination does not significantly perturb the ETM conformation. F20/23 Cβ, F26 Cβ, and T30 Cγ2 show small chemical shift changes (*blue*) of 0.3-0.6 ppm. The spectra were measured at 293 K. (**b**) 1D $^{13}C$-$^{19}F$ REDOR control ($S_0$), dephased (S), and difference (ΔS) spectra. The difference peaks indicate carbons that are in close proximity to a fluorine in a neighboring helix. The broadband REDOR spectra (*left*) show both sidechain and backbone $^{13}C$ signals whereas the Cα-selective REDOR spectra (*right*) detect only Cα signals. (**c**) Representative $^{13}C$-$^{19}F$ REDOR dephasing curves for broadband and Cα-selective C-F REDOR spectra. The $S/S_0$ values have been corrected for the isotopic dilution factor (50%) and

the overlap factor. Best-fit distance curves are shown as solid lines, and lower and upper distance bounds are shown as dashed lines. (**d**) Water-edited 2D $^{15}$N-$^{13}$Cα correlation spectra to detect well hydrated residues. The spectra were measured at 293 K under 11.8 kHz MAS using $^{1}$H-$^{1}$H mixing times of 9 ms (*red*) and 100 ms (*blue*).

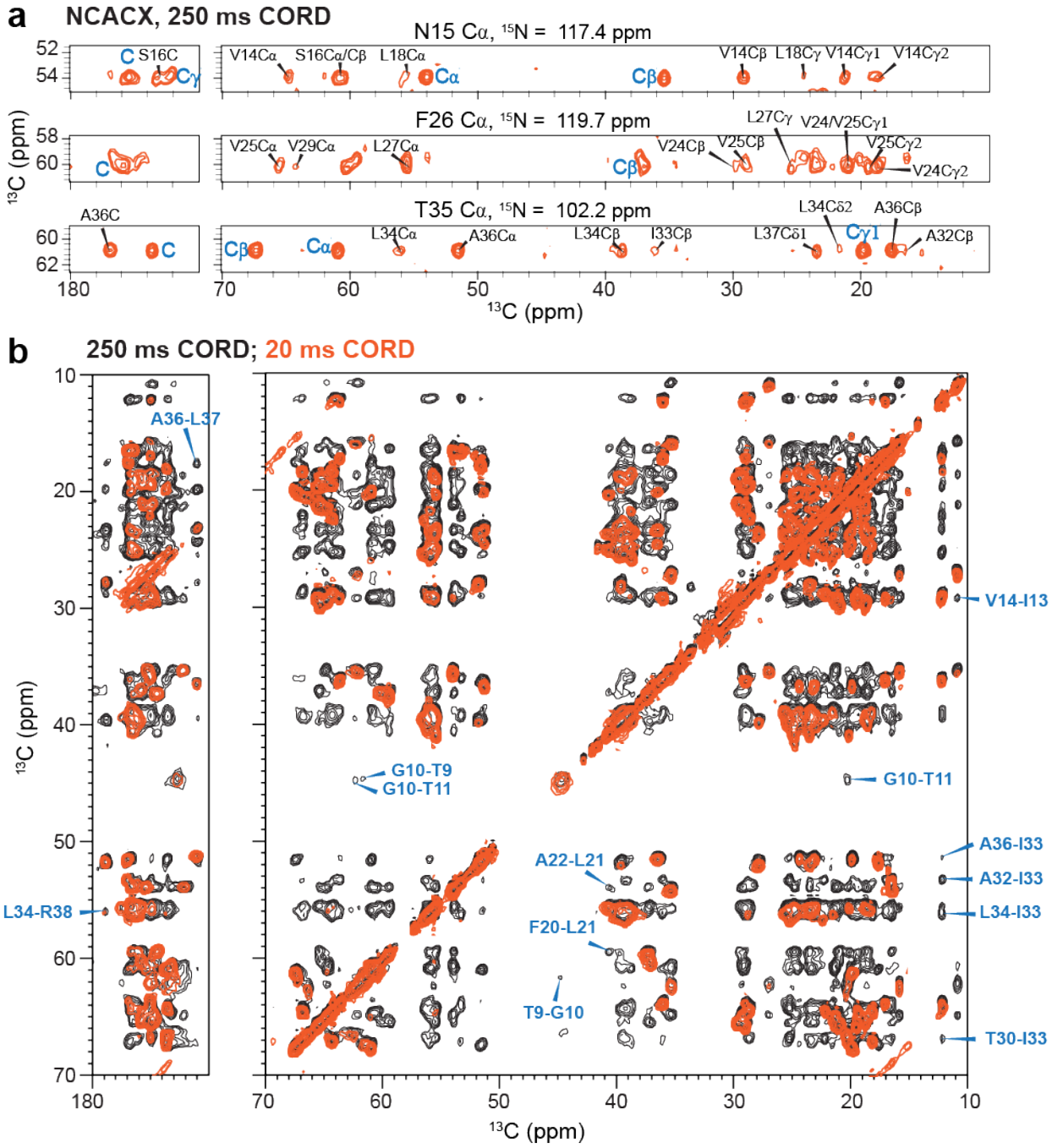


**Figure S6**. Inter-residue correlations obtained from 250 ms $^{13}C$-$^{13}C$ spin diffusion. (**a**) Representative strips from a well-resolved 3D NCACX spectrum recorded with 250 ms $^{13}C$ spin diffusion. Inter-residue cross peaks are assigned in black and intra-residue resonances are marked in blue. (**b**) Overlay of 2D $^{13}C$-$^{13}C$ correlation spectra measured with 250 ms mixing (*black*) and 20 ms (*orange*). Representative inter-residue cross peaks are assigned. All spectra were measured at 293 K under 11.8 kHz MAS.

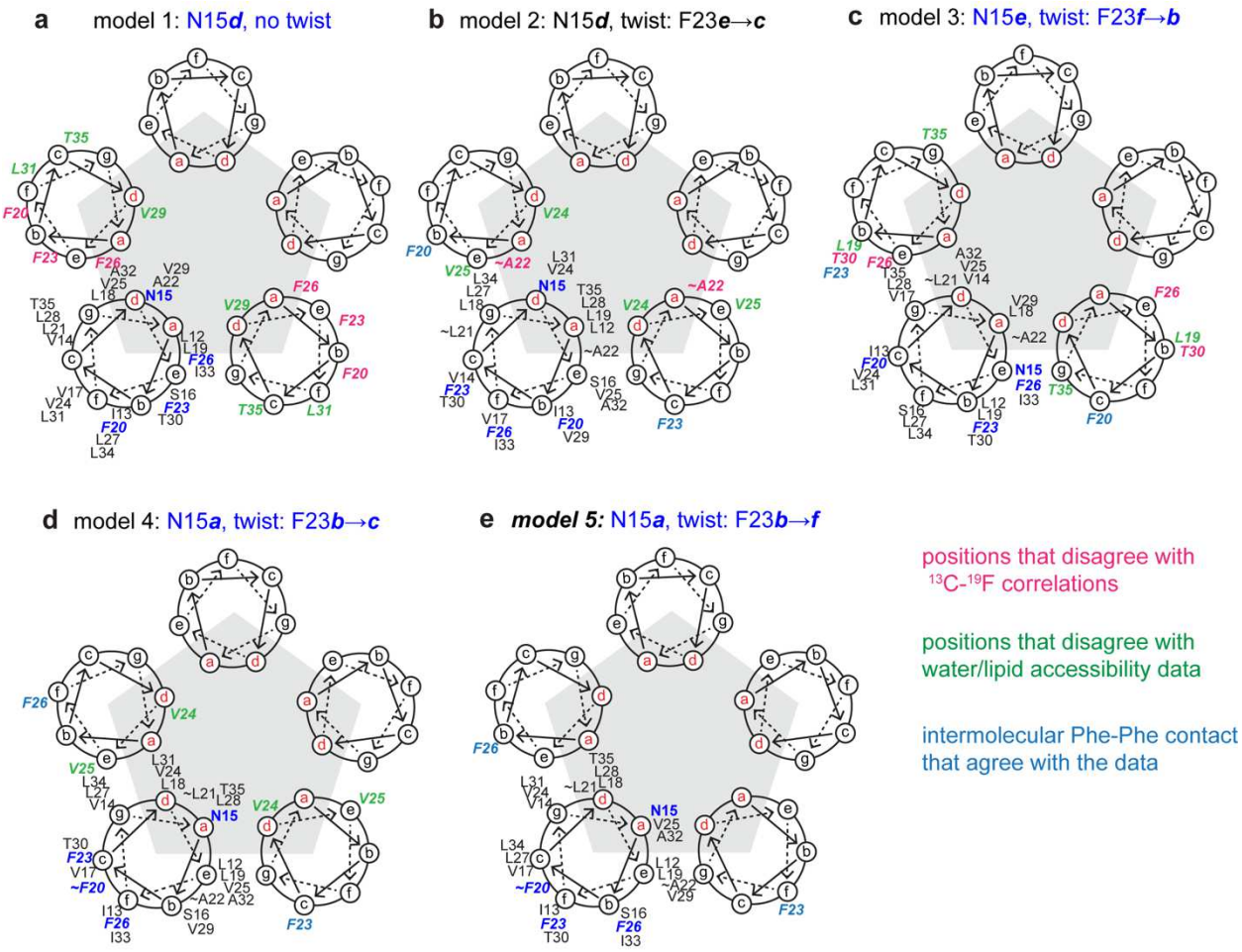


**Figure S7.** ETM pentameric models analyzed for structure calculation. For each model, the heptad repeat positions (*abcdefg*) of every residue from L12 to T35 is indicated on the helical wheel for one subunit. On the two neighboring helices, residue positions that violate measured $^{13}$C-$^{19}$F correlations are shown in pink, while residue positions that violate the water/lipid accessibility data are shown in green. The positions of Phe residues that satisfy the interhelical contacts are shown in blue. (**a**) Model 1 places N15 at heptad position *d* without a twist. (**b**) Model 2 places N15 at *d* with a twist such that F23 moves from *e* to *c*. (**c**) Model 3 places N15 at *e* with a twist such that F23 moves from *f* to *b*. (**d**) Model 4 places N15 at *a* with a twist such that F23 moves from *b* to *c*. (**e**) Model 5 places N15 at *a* with a twist such that F23 moves from *b* to *f*. Model 5 does not violate any experimental data and was thus chosen to disambiguate intermolecular contacts for structure calculation.

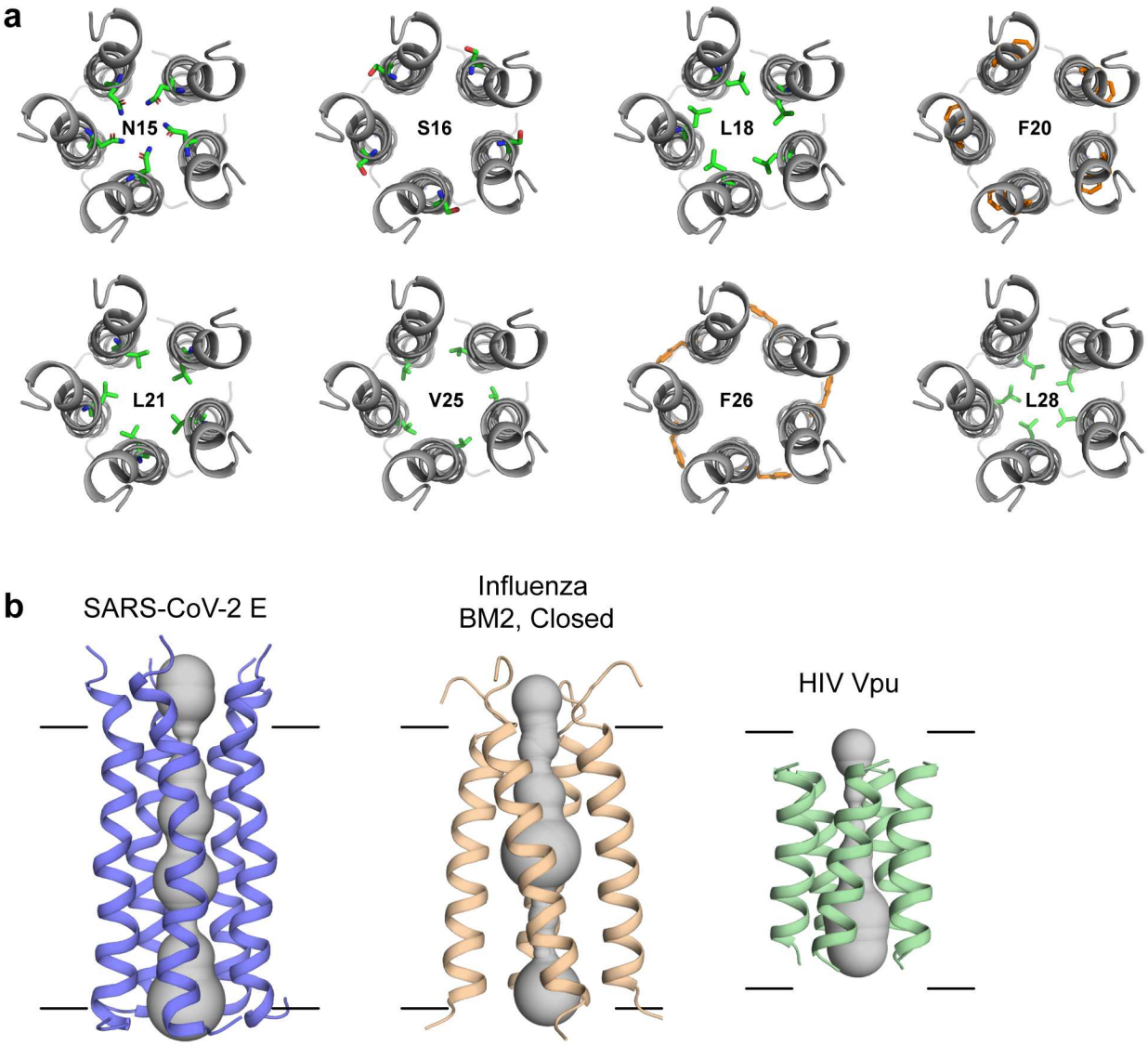


**Figure S8**. Membrane-bound structure of SARS-CoV-2 E TM domain compared to other viroporins. (**a**) Top views (seen from the N-terminus) of various residues in the ETM pentamer. Most residues are hydrophobic, including both pore-facing and lipid-facing residues. (**b**) Comparative HOLE plots of the pentameric ETM channel with the closed state of the tetrameric influenza BM2 proton channel (PDB:6PVR) and the pentameric HIV-1 Vpu channel (PDB: 1PI7). ETM is longer and tighter than BM2 and Vpu and exhibits a smaller helix tilt angle.

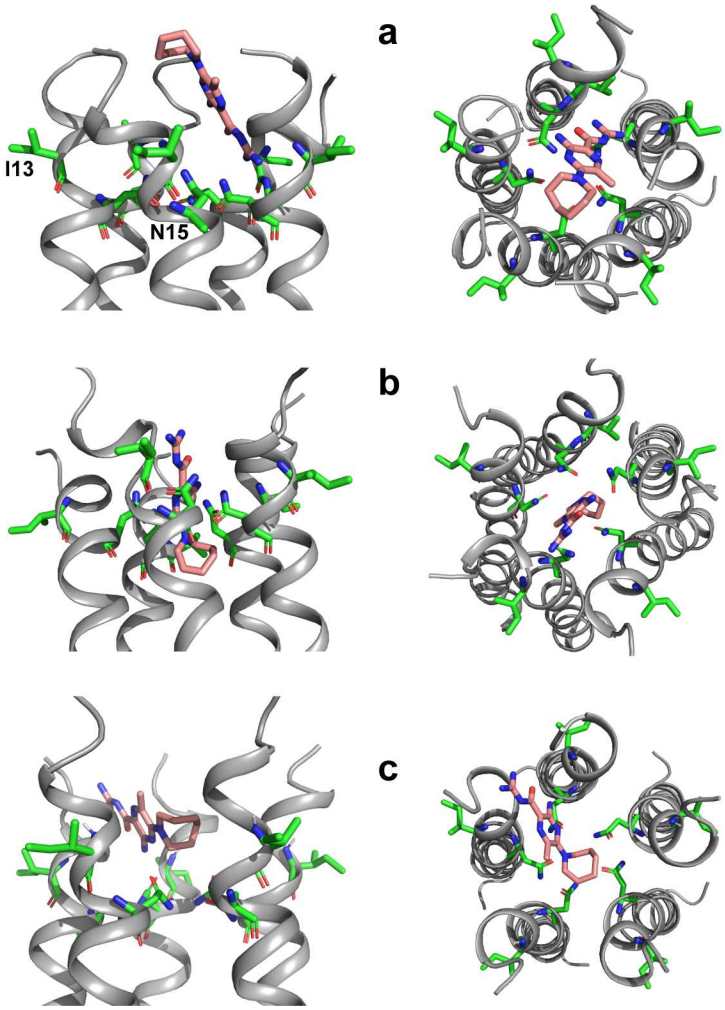


**Figure S9**. Additional docking poses of HMA in SARS-CoV-2 E, shown in sideview (left) and top view from the N-terminus (right). (**a**) Structure with hexamethylene up and HMA vertical, obtained from docking in DMSO. (**b**) Structure with hexamethylene down and HMA vertical, obtained from docking in DMSO. (**c**) Structure with HMA across the channel entrance, bridging two helices, obtained from docking in water. The lipid-facing I13 and pore-occluding N15 are shown in sticks to guide the eye.

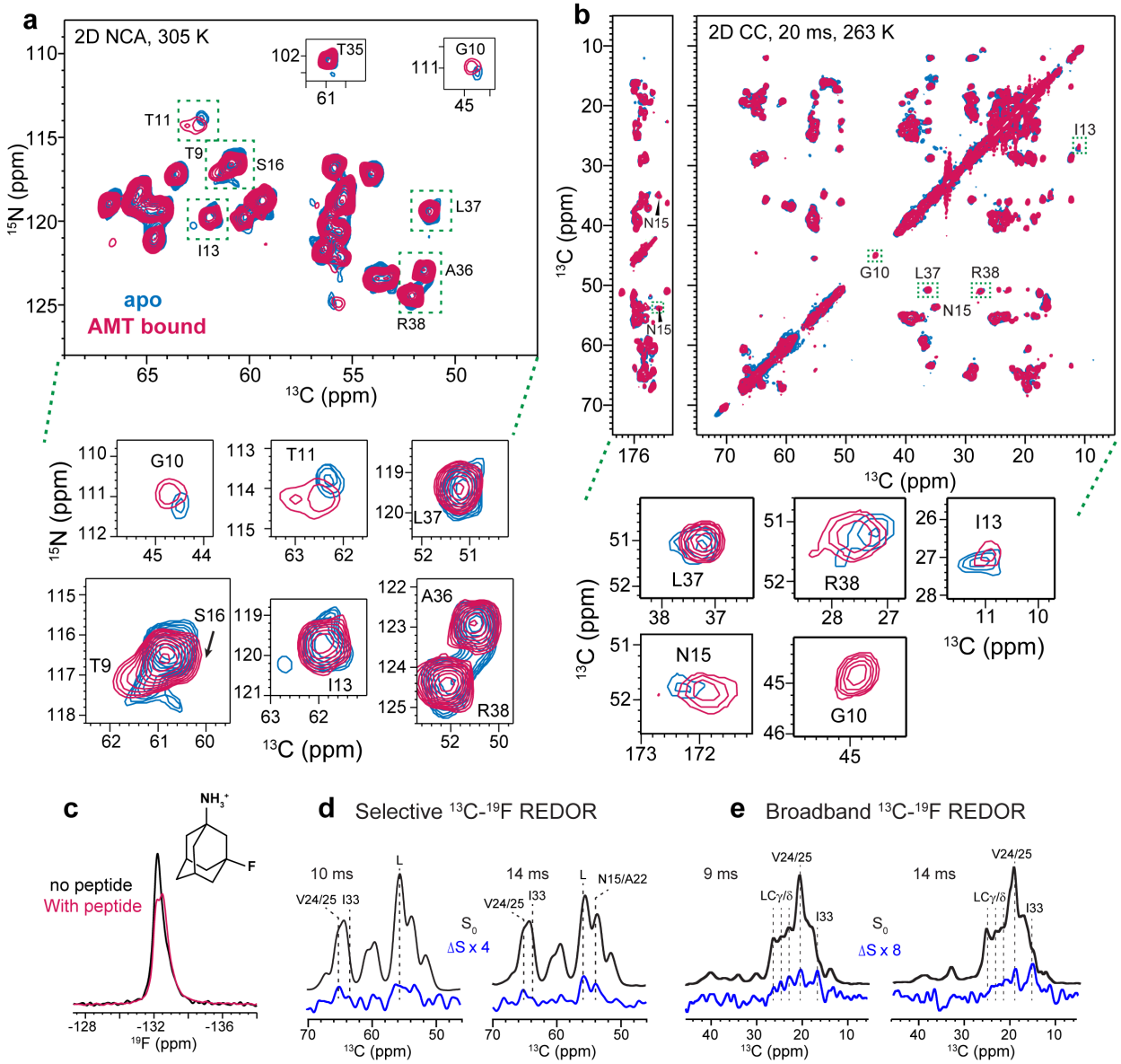


**Figure S10**. Effects of amantadine (Amt) binding on ETM. The peptide is reconstituted in DMPC : DMPG membranes with an Amt : ETM monomer molar ratio is 8 : 1. (**a**) 2D $^{15}$N-$^{13}$Cα correlation spectra of apo (*blue*) and Amt-bound ETM (*magenta*). The spectra were measured at 305 K under 14 kHz MAS. Zoomed-in areas show peaks with significant CSPs. (**b**) 2D $^{13}$C-$^{13}$C correlation spectra with 20 ms mixing of apo (*blue*) and Amt-bound ETM (*magenta*). The spectra were measured at 263 K. Zoomed-in areas shows peaks with significant CSPs. The perturbed residues are concentrated in the N- and C-termini of the protein. (**c**) 1D $^{19}$F direct-polarization spectra of 3F-Amt with and without ETM in DMPX membranes. The spectra were measured at 270 K under 14 kHz MAS. (**d**) $^{13}$Cα selective $^{19}$F-dephased REDOR spectra of Amt-bound ETM in DMPC : DMPG membranes. The ΔS spectra show dephasing at 65.5 ppm, 63.6 ppm, 56 ppm and 54 ppm. (**e**) Broadband $^{13}$C-$^{19}$F REDOR spectra. The ΔS spectra show $^{13}$C dephasing for sidechains that belong to residues that show Cα dephasing in (**d**).

**Table S1.** $^{13}C$ and $^{15}N$ chemical shifts (ppm) of ERGIC-bound ETM at pH 7.5. The $^{13}C$ and $^{15}N$ chemical shift uncertainties are ±0.3 ppm and ±0.5 ppm, respectively.

| Residue | Cα | Cβ | C' | N | Cγ/γ1 | Cγ2 | Cδ/δ1 | Cδ2 | Cε/ Cε1 | Cε2/ ζ | Nδ |
|---|---|---|---|---|---|---|---|---|---|---|---|
| E8 | | | | | 33.6 | | 181.1 | | | | |
| T9 | 61.5 | 67.2 | | 117.5 | | | | | | | |
| G10 | 44.8 | | 172.7 | 110.7 | | | | | | | |
| T11 | 62.5 | 66.5 | 173.4 | 113.5 | | 20.4 | | | | | |
| L12 | 55.7 | 39.4 | | 121.9 | 25.0 | | | | | | |
| I13 | 62.1 | 35.3 | 175.1 | 119.9 | 27.1 | 15.9 | 10.9 | | | | |
| V14 | 64.9 | 29.2 | 174.7 | 119.6 | 21.3 | 18.8 | | | | | |
| N15 | 53.9 | 35.4 | 175.4 | 117.1 | 172.2 | | | | | | 107.7 |
| S16 | 60.9 | 61.0 | 173.2 | 116.4 | | | | | | | |
| V17 | 64.7 | 29.2 | 175.4 | 121.0 | 21.3 | 19.4 | | | | | |
| L18 | 55.6 | 39.0 | 176.7 | 118.6 | 24.7 | | 23.4 | 18.3 | | | |
| L19 | 56.1 | 39.9 | 176.0 | 120.5 | 24.9 | | | | | | |
| F20 | 59.5 | 37.4 | 174.5 | 118.9 | 136.8 | | 129.3 | | 128.3 | | |
| L21 | 55.5 | 40.8 | 176.6 | 118.8 | 24.9 | | 23.6 | 20.2 | | | |
| A22 | 53.9 | 16.5 | 176.5 | 123.5 | | | | | | | |
| F23 | 59.4 | 37.3 | 174.3 | 118.9 | 137.2 | | 129.3 | | 127.3 | | |
| V24 | 65.4 | 29.7 | 175.7 | 118.3 | 21.0 | 18.8 | | | | | |
| V25 | 65.6 | 29.1 | 174.8 | 118.9 | 21.1 | 19.5 | | | | | |
| F26 | 60.2 | 37.0 | 175.7 | 119.7 | 137.0 | | 129.3 | | 128.1 | | |
| L27 | 55.6 | 39.8 | 175.9 | 120.8 | 25.5 | | 23.8 | 18.6 | | | |
| L28 | 55.5 | 39.1 | 176.6 | 118.4 | 23.5 | | 23.4 | 18.8 | | | |
| V29 | 64.3 | 28.7 | 175.0 | 119.4 | 22.2 | 19.4 | | | | | |
| T30 | 66.9 | 64.4 | 173.5 | 119.2 | | 18.2 | | | | | |
| L31 | 56.5 | 39.5 | 176.1 | 121.7 | 25.3 | | 25.2 | 22.3 | | | |
| A32 | 53.3 | 16.5 | 177.0 | 123.6 | | | | | | | |
| I33 | 63.6 | 36.1 | 175.0 | 117.6 | 28.9 | 17.1 | 12.2 | | | | |
| L34 | 55.9 | 38.8 | 176.5 | 117.0 | 25.6 | | 25.5 | 21.5 | | | |
| T35 | 60.9 | 67.4 | 173.6 | 102.2 | | 19.8 | | | | | |
| A36 | 51.6 | 17.6 | 176.9 | 123.1 | | | | | | | |
| L37 | 51.3 | 36.6 | 171.0 | 119.5 | 24.4 | | 23.3 | 19.9 | | | |
| R38 | 51.8 | 27.9 | 178.9 | 124.4 | 23.5 | | 39.6 | | | 157.3 | |

**Table S2**. Interhelical $^{1}H$-$^{1}H$ distance restraints obtained from the NHHC spectra. The direction of the interhelical contact from the $^{15}N$ to the $^{13}C$ is indicated as 'CCW' for counter-clockwise, 'CW' for clockwise, and 'Ambig' for either of the two neighboring helices during structure calculation.

| Source ($^{15}N$) | Sink ($^{13}C$) | Direction | $^{1}H$-$^{1}H$ SD time (us) | Distance (Å) | Lower Error (Å) | Upper Error (Å) |
|---|---|---|---|---|---|---|
| L12N | T11CA | CCW | 500 | 6.0 | 3.0 | 3.0 |
| S16N | L18CA | CCW | 500 | 6.0 | 3.0 | 3.0 |
| V14N | S16CB | CW | 500 | 6.0 | 3.0 | 3.0 |
| A32N | L31CA | CCW | 500 | 6.0 | 3.0 | 3.0 |
| L21N | A22CA | CW | 500 | 6.0 | 3.0 | 3.0 |
| L31N | V29CA | CW | 500 | 6.0 | 3.0 | 3.0 |
| V29N | T30CB | CCW | 1000 | 6.0 | 3.0 | 5.5 |
| S16N | V14CB | CCW | 500 | 6.0 | 3.0 | 3.0 |
| V14N | N15CB | CW | 500 | 6.0 | 3.0 | 3.0 |
| L28N/V29N | T30CA | Ambig | 500 | 6.0 | 3.0 | 3.0 |
| V25N | L21CB | CCW | 1000 | 6.0 | 3.0 | 5.5 |
| A22N | F20CB/F23CB | CCW | 1000 | 6.0 | 3.0 | 5.5 |
| S16N | T11CG2/L21CD2 | CCW | 1000 | 6.0 | 3.0 | 5.5 |
| N15N | V14CA/V17CA | CCW | 1000 | 6.0 | 3.0 | 5.5 |
| L34N | A36CA | CW | 1000 | 6.0 | 3.0 | 5.5 |
| I33N/L34N | T35CA | Ambig | 1000 | 6.0 | 3.0 | 5.5 |
| L21N | A22CB | CW | 1000 | 6.0 | 3.0 | 5.5 |
| L27N | V25CA | CW | 1000 | 6.0 | 3.0 | 5.5 |
| A22N | V17CB | CCW | 1000 | 6.0 | 3.0 | 5.5 |
| A32N/A36N | I33CG2 | Ambig | 1000 | 6.0 | 3.0 | 5.5 |
| L27N | F26CA | CW | 1000 | 6.0 | 3.0 | 5.5 |
| L31N | L37CA | CW | 1000 | 6.0 | 3.0 | 5.5 |
| T30N/L37N | R38CA | Ambig | 1000 | 6.0 | 3.0 | 5.5 |
| L37N | T35CB | Ambig | 1000 | 6.0 | 3.0 | 5.5 |
| L21N/F23N | V25CA | CCW | 1000 | 6.0 | 3.0 | 5.5 |
| A32N | A36CA/R38CA | Ambig | 1000 | 6.0 | 3.0 | 5.5 |
| L34N | I33CG1 | Ambig | 1000 | 6.0 | 3.0 | 5.5 |
| L31N | V29CB | CW | 1000 | 6.0 | 3.0 | 5.5 |
| L27N | V29CB | CW | 1000 | 6.0 | 3.0 | 5.5 |
| N15N | S16CA | CW | 500 | 6.0 | 3.0 | 3.0 |
| S16N | L21CB | CCW | 1000 | 6.0 | 3.0 | 5.5 |
| L19N | V17CA | CCW | 500 | 6.0 | 3.0 | 3.0 |
| N15N | L18CA | Ambig | 500 | 6.0 | 3.0 | 3.0 |
| S16N | L18CB | CCW | 500 | 6.0 | 3.0 | 3.0 |
| V17N | L18CA/L19CA | Ambig | 500 | 6.0 | 3.0 | 3.0 |
| L19N | S16CA | CW | 500 | 6.0 | 3.0 | 3.0 |
| L31N | I33CG1 | CW | 500 | 6.0 | 3.0 | 3.0 |
| A32N | T35CG2 | Ambig | 500 | 6.0 | 3.0 | 3.0 |
| A32N/R38N | I33CG2 | Ambig | 500 | 6.0 | 3.0 | 3.0 |
| S16N | L18CD2 | CCW | 500 | 6.0 | 3.0 | 3.0 |

| | | | | | | |
|---|---|---|---|---|---|---|
| I33N/L34N | T35CB | Ambig | 1000 | 6.0 | 3.0 | 5.5 |
| L31N | A32CB | CW | 1000 | 6.0 | 3.0 | 5.5 |
| A32N | A32CB | Ambig | 1000 | 6.0 | 3.0 | 5.5 |
| A32N/R38N | A36CA | Ambig | 1000 | 6.0 | 3.0 | 5.5 |
| T35N | T35CG2 | Ambig | 1000 | 6.0 | 3.0 | 5.5 |
| L31N | I33CB | CW | 1000 | 6.0 | 3.0 | 5.5 |
| L31N | T30CA | Ambig | 1000 | 6.0 | 3.0 | 5.5 |
| A32N | T35CA | Ambig | 1000 | 6.0 | 3.0 | 5.5 |
| A32N | T35CB | Ambig | 1000 | 6.0 | 3.0 | 5.5 |
| A32N/R38N | L34CG | Ambig | 1000 | 6.0 | 3.0 | 5.5 |
| A22N | F20C/F23C | CCW | 1000 | 6.0 | 3.0 | 5.5 |
| L28N | T30CG2 | Ambig | 1000 | 6.0 | 3.0 | 5.5 |

**Table S3**. Interhelical $^{13}C$-$^{19}F$ distance restraints. Positive contacts are $^{13}C$ sites that show significant REDOR dephasing while negative contacts are sites that do not show significant REDOR dephasing and are thus far from all $^{19}F$ spins. The direction of the interhelical contact from the $^{19}F$ spin to $^{13}C$ is indicated as 'CCW' for counter-clockwise, The experiments that yielded these constraints include broadband $^{13}C$-$^{19}F$ REDOR (BB), C$\alpha$-selective $^{13}C$-$^{19}F$ REDOR (C$\alpha$-sel), and water-edited and lipid-edited (Water/lipid) experiments.

| Dephasing Atom ($^{19}F$) | Dephased Site ($^{13}C$) | Direction | Experiment | Distance (Å) | Lower Error (A) | Upper Error (A) | Contact Type |
|---|---|---|---|---|---|---|---|
| F20HZ | I13CA | Ambig | 2D Cα-sel | 12.0 | 4.7 | 38.0 | negative |
| F20HZ | N15CA | Ambig | 2D Cα-sel | 9.1 | 2.0 | 40.9 | negative |
| F20HZ | S16CA | Ambig | 2D Cα-sel | 12.0 | 4.0 | 38.0 | negative |
| F20HZ | V17CA | Ambig | 2D Cα-sel | 7.7 | 2.0 | 2.0 | positive |
| F26HZ | F23CA | CCW | 2D Cα-sel | 6.8 | 2.0 | 2.0 | positive |
| F20HZ | L21CA | Ambig | 2D Cα-sel | 6.6 | 2.0 | 2.0 | positive |
| F20HZ/F23HZ | A22CA | CW | 2D Cα-sel | 6.5 | 2.0 | 2.0 | positive |
| F26HZ | V24CA | CCW | 2D Cα-sel | 6.7 | 2.0 | 2.0 | positive |
| F23HZ | V25CA | CW | 2D Cα-sel | 6.7 | 2.0 | 2.0 | positive |
| F23HZ | F26CA | CW | 2D Cα-sel | 6.5 | 2.6 | 2.0 | positive |
| F20HZ/F23HZ/ F26HZ | L18CA/L27C A/L28CA | Ambig | 2D Cα-sel | 7.2 | 2.0 | 2.0 | positive |
| F23HZ/F26HZ | V29CA | Ambig | 2D Cα-sel | 7.7 | 2.0 | 2.0 | positive |
| F26HZ | T30CB | CCW | 2D Cα-sel | 7.1 | 2.0 | 2.0 | positive |
| F26HZ | T30CA | Ambig | 2D Cα-sel | 8.5 | 2.0 | 41.5 | negative |
| F26HZ | L31CA | Ambig | 2D Cα-sel | 7.5 | 2.0 | 42.5 | negative |
| F26HZ | A32CA | Ambig | 2D Cα-sel | 9.5 | 2.0 | 40.5 | negative |
| F26HZ | I33CA | Ambig | 2D Cα-sel | 10.9 | 2.7 | 39.1 | negative |
| F26HZ | T35CB | Ambig | 2D Cα-sel | 12.0 | 4.8 | 38.0 | negative |
| F26HZ | T35CA | Ambig | 2D Cα-sel | 12.0 | 4.5 | 38.0 | negative |
| F20HZ | I13CD1 | Ambig | 1D BB | 12.0 | 2.0 | 38.0 | negative |
| F20HZ | I13CG2 | Ambig | 1D BB | 8.3 | 2.0 | 41.7 | negative |
| F20HZ/F23HZ/ F26HZ | L21CB | Ambig | 1D BB | 6.1 | 2.0 | 2.0 | positive |
| F20HZ | A22CB | CW | 1D BB | 5.7 | 2.0 | 2.0 | positive |
| F26HZ | T30CG2 | CCW | 1D BB | 5.9 | 2.0 | 2.0 | positive |
| F26HZ | I33CD1 | Ambig | 1D BB | 12.0 | 2.0 | 38.0 | negative |
| F26HZ | A36CA | Ambig | 1D Cα-sel | 12.0 | 2.0 | 38.0 | negative |
| F26HZ | L37CA | Ambig | 1D Cα-sel | 12.0 | 2.0 | 38.0 | negative |
| F26HZ | R38CA | Ambig | 1D Cα-sel | 12.0 | 2.0 | 38.0 | negative |
| F26HZ | R38CB | Ambig | 1D BB | 12.0 | 3.4 | 38.0 | negative |
| F26HZ | R38CZ | Ambig | 1D BB | 12.0 | 3.4 | 38.0 | negative |
| F23HZ | F26CE#/F26 CZ | CW | 1D BB | 3.3 | 2.0 | 2.0 | positive |
| F26HZ | L31CD2 | CCW | 1D BB | 6.4 | 2.0 | 2.0 | positive |
| F26HZ | F26HZ | Ambig | Water/lipid | 12.0 | 3.0 | 38.0 | negative |
| F20HZ | F20HZ | Ambig | Water/lipid | 12.0 | 3.0 | 38.0 | negative |
| F23HZ | F23HZ | Ambig | Water/lipid | 12.0 | 3.0 | 38.0 | negative |

**Table S4.** XPLOR-NIH parameters for ETM structure calculations.

| XPLOR-NIH Potential | Experimental Basis | Restraints per monomer | Round 1 Scale Factor | Round 2 Scale Factor | Best model energy (kcal/mol) |
|---|---|---|---|---|---|
| PosDiffPot (ncs) | Single set of chemical shifts | - | 100 | 100 | 0.57 |
| DistSymmPot | Single set of chemical shifts | - | 100 | 100 | 0.17 |
| CDIH (dihedral angles) | TALOS-N predictions | 56 | 400 | 400 | 0.97 |
| NOE | Intermolecular NHHC contacts | 52 | 0.01-20 | 0.5-30 | 128.70 |
| NOE | Intermolecular $^{13}C$-$^{19}F$ REDOR | 35 | 0.01-20 | 0.5-30 | |
| NOE | Intramolecular inter-residue $^{13}C$-$^{13}C$ contacts | 196 | 0 | 0.17-10 | |
| HBDB | α-helical TM for residues 13-19, 23-34 | 11 | 1 | 1 | -121.52 |
| TorsionDB | Database favored side-chain rotamers | - | 0.0001-0.1 | 0.01-1 | 2771.91 |
| BOND | Standard bond lengths | - | 1 | 1 | 19.56 |
| ANGL | Standard bond angles | - | 0.4-1 | 0.4-1 | 130.89 |
| IMPR | Standard bond geometry | - | 0.1-1 | 0.1-1 | 14.41 |
| RepelPot | Non-bonded atomic radii repulsion | - | 0.004-4 | 0.006-6 | 57.33 |

**Table S5**. Detailed solid-state NMR experimental parameters for bilayer-bound ETM.

| Sample | Experiment | NMR Parameters | Experimental Time |
|---|---|---|---|
| pH 7.5, ERGIC, U-$^{13}$C, $^{15}$N-labeled ETM | 2D CC short CORD, high T | $B_0$ = 21.1 T; $T_{bearing}$ = 293 K; $\nu_{MAS}$ = 11.8 kHz, ns = 72, $\tau_{rd}$ = 1.7 s, $t_{1,max}$ = 4.4 ms; $t_{1,inc}$ = 25.0 µs; $\tau_{dwell}$ = 6.0 µs; $\tau_{acq}$ = 10.2 ms; $\tau_{HC}$ = 0.5 ms; $\tau_{CORD}$ = 20 ms; $\nu_{1Hacq}$ = 71 kHz | 14 hrs |
| | 2D CC short CORD, low T | $B_0$ = 21.1 T; $T_{bearing}$ = 263 K; $\nu_{MAS}$ = 11.8 kHz, ns = 64, $\tau_{rd}$ = 1.7 s, $t_{1,max}$ = 5.0 ms; $t_{1,inc}$ = 25.0 µs; $\tau_{dwell}$ = 6.0 µs; $\tau_{acq}$ = 10.2 ms; $\tau_{HC}$ = 0.5 ms; $\tau_{CORD}$ = 20 ms; $\nu_{1Hacq}$ = 71 kHz | 12 hrs |
| | 2D CC long CORD | $B_0$ = 21.1 T; $T_{bearing}$ = 293 K; $\nu_{MAS}$ = 11.8 kHz, ns = 160, $\tau_{rd}$ = 1.6 s , $t_{1,max}$ = 5.0 ms; $t_{1,inc}$ = 22.1 µs; $\tau_{dwell}$ = 6.0 µs; $\tau_{acq}$ = 12.8 ms; $\tau_{HC}$ = 0.5 ms; $\tau_{CORD}$ = 250 ms; $\nu_{1Hacq}$ = 71 kHz | 30 hrs |
| | 2D NCA, high T | $B_0$ = 21.1 T; $T_{bearing}$ = 293 K; $\nu_{MAS}$ = 11.8 kHz, ns = 32, $\tau_{rd}$ = 2.0 s, $t_{1,max}$ = 8.9 ms; $t_{1,inc}$ = 127 µs; $\tau_{dwell}$ = 5 µs; $\tau_{acq}$ = 15.4 ms; $\tau_{HN}$ = 0.75 ms; $\tau_{CN}$ = 4 ms; $\nu_{15NspecificCP}$ = 30 kHz; $\nu_{13CspecificCP}$ = 18 kHz; $\nu_{1HspecificCP}$ = 80 kHz; $\nu_{1Hacq}$ = 71 kHz | 2.5 hrs |
| | 2D NCA, low T | $B_0$ = 21.1 T; $T_{bearing}$ = 263 K; $\nu_{MAS}$ = 11.8 kHz, ns = 32, $\tau_{rd}$ = 2.0 s, $t_{1,max}$ = 8.9 ms; $t_{1,inc}$ = 127 µs; $\tau_{dwell}$ = 5 µs; $\tau_{acq}$ = 15.4 ms; $\tau_{HN}$ = 0.75 ms; $\tau_{CN}$ = 4 ms; $\nu_{15NspecificCP}$ = 30 kHz; $\nu_{13CspecificCP}$ = 18 kHz; $\nu_{1HspecificCP}$ = 80 kHz; $\nu_{1Hacq}$ = 71 kHz | 2.5 hrs |
| | 3D NCACX, 28 ms CORD | $B_0$ = 21.1 T; $T_{bearing}$ = 293 K; $\nu_{MAS}$ = 11.8 kHz, ns = 8, $\tau_{rd}$ = 2.0 s, $t_{1,max}$ = 5.9 ms; $t_{1,inc}$ = 169.5 µs; $t_{2,max}$ = 4 ms; $t_{2,inc}$ = 100 µs; $\tau_{dwell}$ = 5 µs; $\tau_{acq}$ = 12.8 ms; $\tau_{HN}$ = 0.75 ms; $\tau_{CN}$ = 4 ms; $\nu_{15NspecificCP}$ = 30 kHz; $\nu_{13CspecificCP}$ = 18 kHz; $\tau_{CORD}$ = 28 ms; $\nu_{1HspecificCP}$ = 80 kHz; $\nu_{1Hacq}$ = 71 kHz | 25 hrs |
| | 3D NCACX, 250 ms CORD | $B_0$ = 21.1 T; $T_{bearing}$ = 293 K; $\nu_{MAS}$ = 11.8 kHz, ns = 24, $\tau_{rd}$ = 2.2 s, $t_{1,max}$ = 4.7 ms; $t_{1,inc}$ = 169.5 µs; $t_{2,max}$ = 3.7 ms; $t_{2,inc}$ = 100 µs; $\tau_{dwell}$ = 5 µs; $\tau_{acq}$ = 12.8 ms; $\tau_{HN}$ = 0.75 ms; $\tau_{CN}$ = 4 ms; $\nu_{15NspecificCP}$ = 30 kHz; $\nu_{13CspecificCP}$ = 18 kHz; $\tau_{CORD}$ = 250 ms; $\nu_{1HspecificCP}$ = 80 kHz; $\nu_{1Hacq}$ = 71 kHz | 69 hrs |
| | 3D NCOCX, 37 ms CORD | $B_0$ = 21.1 T; $T_{bearing}$ = 293 K; $\nu_{MAS}$ = 11.8 kHz, ns = 16, $\tau_{rd}$ = 2.0 s, $t_{1,max}$ = 5.9 ms; $t_{1,inc}$ = 169.5 µs; $t_{2,max}$ = 4.4 ms; $t_{2,inc}$ = 169.5 µs; $\tau_{dwell}$ = 5 µs; $\tau_{acq}$ = 12.8 ms; $\tau_{HN}$ = 0.75 ms; $\tau_{CN}$ = 4 ms; $\nu_{15NspecificCP}$ = 30 kHz; $\nu_{13CspecificCP}$ = 42 kHz; $\tau_{CORD}$ = 37 ms; $\nu_{1HspecificCP}$ = 80 kHz; $\nu_{1Hacq}$ = 71 kHz | 35 hrs |
| | 3D CONCA | $B_0$ = 21.1 T; T = 293 K; $\nu_{MAS}$ = 11.8 kHz, ns = 16, $\tau_{rd}$ = 2.0 s, $t_{1,max}$ = 4.1 ms; $t_{1,inc}$ = 169.5 µs; $t_{2,max}$ = 5.8 ms; $t_{2,inc}$ = 169.5 µs; $\tau_{dwell}$ =5 µs; $\tau_{acq}$ = 12.9 ms; $\tau_{HC}$ = 1 ms; $\tau_{CN}$ = 4 ms; $\nu_{15NspecificCP}$ = 30 kHz; $\nu_{13CspecificCP}$ = 42 kHz; $\tau_{NC}$ = 4 ms; $\nu_{15NspecificCP}$ = 30 kHz; $\nu_{13CspecificCP}$ = 18 kHz; $\nu_{1HspecificCP}$ = 80 kHz; $\nu_{1Hacq}$ = 71 kHz | 30 hrs |
| | 1D $^{13}$C CP | $B_0$ = 21.1 T; $\nu_{MAS}$ = 11.8 kHz, ns = 1024, $\tau_{rd}$ = 1.5 s, $\tau_{dwell}$ = 6 µs; $\tau_{acq}$ = 12.3 ms; $\tau_{HC}$ = 0.5 ms; $\nu_{1Hacq}$ = 71 kHz | 0.4 hrs |
| | 1D $^{15}$N CP | $B_0$ = 21.1 T; $\nu_{MAS}$ = 11.8 kHz, ns = 1024, $\tau_{rd}$ = 1.6 s, $\tau_{dwell}$ = 12 µs; $\tau_{acq}$ = 12.3 ms; $\tau_{HN}$ = 0.75 ms; $\nu_{1Hacq}$ = 71 kHz | 0.4 hrs |
| | 1D water-edited $^{13}$C CP with 9 ms $^{1}$H SD | $B_0$ = 21.1 T; $T_{bearing}$ = 293 K; $\nu_{MAS}$ = 11.8 kHz, ns = 1024, $\tau_{rd}$ = 2.0 s, $\tau_{dwell}$ = 5 µs; $\tau_{acq}$ = 12.8 ms; $\tau_{1Hexc}$ = 1.7 ms; $\tau_{1HSD}$ = 9 ms; $\tau_{HC}$ = 0.5 ms; $\nu_{1Hacq}$ = 71 kHz | 0.5 hrs |
| | 1D water-edited $^{13}$C CP with 100 ms $^{1}$H SD | $B_0$ = 21.1 T; $T_{bearing}$ = 293 K; $\nu_{MAS}$ = 11.8 kHz, ns = 1024, $\tau_{rd}$ = 2.0 s, $\tau_{dwell}$ = 5 µs; $\tau_{acq}$ = 12.8 ms; $\tau_{1Hexc}$ = 1.7 ms; $\tau_{1HSD}$ = 100 ms; $\tau_{HC}$ = 0.5 ms; $\nu_{1Hacq}$ = 71 kHz | 0.5 hrs |
| | 2D water-edited NCA with 9 ms $^{1}$H SD | $B_0$ = 21.1 T; $T_{bearing}$ = 293 K; $\nu_{MAS}$ = 11.8 kHz, ns = 640, $\tau_{rd}$ = 2.0 s, $t_{1,max}$ = 8.5 ms; $t_{1,inc}$ = 169.5 µs; $\tau_{dwell}$ = 5 µs; $\tau_{acq}$ = 12.8 ms; $\tau_{1Hexc}$ = 1.7 ms; $\tau_{1HSD}$ = 9 ms; $\tau_{HN}$ = 0.75 ms; $\tau_{NC}$ = 4 ms; $\nu_{15NspecificCP}$ = 30 kHz; $\nu_{13CspecificCP}$ = 18 kHz; $\nu_{1HspecificCP}$ = 80 kHz; $\nu_{1Hacq}$ = 71 kHz | 46 hrs |

| | | | |
|---|---|---|---|
| | 2D water-edited NCA with 100 ms $^{1}$H SD | $B_0$ = 21.1 T; $T_{bearing}$ = 293 K; $\nu_{MAS}$ = 11.8 kHz, ns = 384, $\tau_{rd}$ = 2.0 s, $t_{1,max}$ = 8.5 ms; $t_{1,inc}$ = 169.5 µs; $\tau_{dwell}$ = 5 µs; $\tau_{acq}$ = 12.8 ms; $\tau_{1Hexc}$ = 1.7 ms; $\tau_{1HSD}$ = 100 ms; $\tau_{HN}$ = 0.75 ms; $\tau_{NC}$ = 4 ms; $\nu_{15NspecificCP}$ = 30 kHz; $\nu_{13CspecificCP}$ = 18 kHz; $\nu_{1HspecificCP}$ = 80 kHz; $\nu_{1Hacq}$ = 71 kHz | 23 hrs |
| | 1D lipid-edited $^{13}$C CP with 10 ms $^{1}$H SD | $B_0$ = 18.8 T; $T_{bearing}$ = 290 K; $\nu_{MAS}$ = 14 kHz, ns = 73728, $\tau_{rd}$ = 1.6 s, $\tau_{dwell}$ = 6 µs; $\tau_{acq}$ = 12.3 ms; $\tau_{1Hexc}$ = 2.86 ms; $\tau_{1HSD}$ = 10 ms; $\tau_{HC}$ = 0.5 ms; $\nu_{1Hacq}$ = 71 kHz | 35 hrs |
| | 1D lipid-edited $^{13}$C CP with 100 ms $^{1}$H SD | $B_0$ = 18.8 T; $T_{bearing}$ = 290 K; $\nu_{MAS}$ = 14 kHz, ns = 26624, $\tau_{rd}$ = 1.6 s, $\tau_{dwell}$ = 6 µs; $\tau_{acq}$ = 12.3 ms; $\tau_{1Hexc}$ = 2.86 ms; $\tau_{1HSD}$ = 100 ms; $\tau_{HC}$ = 0.5 ms; $\nu_{1Hacq}$ = 71 kHz | 12 hrs |
| | | | |
| pH 7.5, ERGIC, 1 : 1 $^{15}$N-labeled : $^{13}$C-labeled ETM | NHHC with 0.5 ms $^{1}$H SD | $B_0$ = 18.8 T; $T_{bearing}$ = 290 K; $\nu_{MAS}$ = 14 kHz, ns = 1792, $\tau_{rd}$ = 1.7 s, $t_{1,max}$ = 5.7 ms; $t_{1,inc}$ = 142.9 µs; $\tau_{dwell}$ = 6 µs; $\tau_{acq}$ = 10.8 ms; $\tau_{1HSD}$ = 0.5 ms; $\tau_{HN}$ = 0.75 ms; $\tau_{NH}$ = 0.75 ms; $\tau_{HC}$ = 0.5 ms; $\nu_{1Hacq}$ = 71 kHz | 68 hrs |
| | NHHC with 1 ms $^{1}$H SD | $B_0$ = 18.8 T; $T_{bearing}$ = 290 K; $\nu_{MAS}$ = 14 kHz, ns = 2176, $\tau_{rd}$ = 1.7 s, $t_{1,max}$ = 5.7 ms; $t_{1,inc}$ = 142.9 µs; $\tau_{dwell}$ = 6 µs; $\tau_{acq}$ = 10.8 ms; $\tau_{1HSD}$ = 1 ms; $\tau_{HN}$ = 0.75 ms; $\tau_{NH}$ = 0.75 ms; $\tau_{HC}$ = 0.5 ms; $\nu_{1Hacq}$ = 71 kHz | 87 hrs |
| | | | |
| pH 7.5, ERGIC, 1 : 1, 4-$^{19}$F-Phe : U-$^{13}$C, $^{15}$N ETM | Broadband 1D $^{13}$C-$^{19}$F REDOR, 5.7 ms (S and $S_0$ pair) | $B_0$ = 14.1 T; $T_{bearing}$ = 293 K; $\nu_{MAS}$ = 14 kHz, ns = 6144, $\tau_{rd}$ = 1.6 s, $\tau_{dwell}$ = 8 µs; $\tau_{acq}$ = 16.4 ms; $\tau_{HC}$ = 0.5 ms; $\tau_{CFREDOR}$=5.7 ms; $\nu_{1HREDOR}$ = 117 kHz; $\nu_{1Hacq}$ = 71 kHz | 5.5 hrs |
| | 1D Cα-sel $^{13}$C-$^{19}$F REDOR, 10.3 ms (S and $S_0$ pair) | $B_0$ = 14.1 T; $T_{bearing}$ = 293 K; $\nu_{MAS}$ = 14 kHz, ns = 2048, $\tau_{rd}$ = 1.8 s, $\tau_{dwell}$ = 8 µs; $\tau_{acq}$ = 16.4 ms; $\tau_{13Casel}$ = 286 µs; $\tau_{HC}$ = 0.5 ms; $\tau_{CFREDOR}$=10.3 ms; $\nu_{1HREDOR}$ = 117 kHz; $\nu_{1Hacq}$ = 71 kHz | 2 hrs |
| | 2D $^{13}$C-$^{13}$C resolved $^{13}$C-$^{19}$F REDOR, 10.3 ms (S and $S_0$ pair) | $B_0$ = 14.1 T; $T_{bearing}$ = 293 K; $\nu_{MAS}$ = 14 kHz, ns = 448, $\tau_{rd}$ = 1.8 s, $t_{1,max}$ = 5.4 ms; $t_{1,inc}$ = 64 µs; $\tau_{dwell}$ = 8 µs; $\tau_{acq}$ = 14.3 ms; $\tau_{13Casel}$ = 286 µs; $\tau_{HC}$ = 0.4 ms; $\tau_{CFREDOR}$=10.3 ms; $\nu_{1HREDOR}$ = 117 kHz; $\nu_{1Hacq}$ = 71 kHz | 76 hrs |
| | 2D $^{13}$C-$^{19}$F double-quantum CP correlation | $B_0$ = 14.1 T; $T_{bearing}$ = 270 K; $\nu_{MAS}$ = 38 kHz, ns = 592, $\tau_{rd}$ = 2.0 s, $t_{1,max}$ = 3.7 ms; $t_{1,inc}$ = 33 µs; $\tau_{dwell}$ = 3 µs; $\tau_{acq}$ = 6.1 ms; $\tau_{HC}$ = 1 ms; $\tau_{CF}$ = 7 ms; $\nu_{19F-CP}$ = 13 kHz; $\nu_{13C-CP}$ = 25 kHz; $\nu_{1H-CP}$ = 117 kHz; $\nu_{1Hacq}$ = 71 kHz | 79 hrs |
| | | | |
| pH 7.5, DMPX | 1D $^{13}$C CP | $B_0$ = 18.8 T; $\nu_{MAS}$ = 14 kHz, ns = 1024, $\tau_{rd}$ = 1.5 s, $\tau_{dwell}$ = 6 µs; $\tau_{acq}$ = 12.3 ms; $\tau_{HC}$ = 0.5 ms; $\nu_{1Hacq}$ = 71 kHz | 0.4 hrs |
| | 1D $^{13}$C DP | $B_0$ = 18.8 T; $\nu_{MAS}$ = 14 kHz, ns = 1024, $\tau_{rd}$ = 2.0 s, $\tau_{dwell}$ = 6 µs; $\tau_{acq}$ = 12.3 ms; $\nu_{1Hacq}$ = 71 kHz | 0.5 hrs |
| | 1D $^{15}$N CP | $B_0$ = 18.8 T; $\nu_{MAS}$ = 14 kHz, ns = 1024, $\tau_{rd}$ = 1.6 s, $\tau_{dwell}$ = 15 µs; $\tau_{acq}$ = 12 ms; $\tau_{HN}$ = 0.75 ms; $\nu_{1Hacq}$ = 71 kHz | 0.4 hrs |
| | 2D CC short CORD, high T | $B_0$ = 18.8 T; $T_{bearing}$ = 305 K; $\nu_{MAS}$ = 14 kHz, ns = 96, $\tau_{rd}$ = 1.6 s, $t_{1,max}$ = 6.2 ms; $t_{1,inc}$ = 25.0 µs; $\tau_{dwell}$ = 6.0 µs; $\tau_{acq}$ = 12.2 ms; $\tau_{HC}$ = 0.5 ms; $\tau_{CORD}$ = 20 ms; $\nu_{1Hacq}$ = 71 kHz | 17 hrs |
| | 2D CC short CORD, low T | $B_0$ = 18.8 T; $T_{bearing}$ = 263 K; $\nu_{MAS}$ = 14 kHz, ns = 96, $\tau_{rd}$ = 1.6 s, $t_{1,max}$ = 6.2 ms; $t_{1,inc}$ = 25.0 µs; $\tau_{dwell}$ = 10.0 µs; $\tau_{acq}$ = 12.2 ms; $\tau_{HC}$ = 0.5 ms; $\tau_{CORD}$ = 20 ms; $\nu_{1Hacq}$ = 71 kHz | 17 hrs |
| | 2D NC TEDOR | $B_0$ = 18.8 T; $T_{bearing}$ = 305 K; $\nu_{MAS}$ = 14 kHz, ns = 256, $\tau_{rd}$ = 2.0 s, $t_{1,max}$ = 10 ms; $t_{1,inc}$ = 142.9 µs; $\tau_{dwell}$ = 6 µs; $\tau_{acq}$ = 12.3 ms; $\tau_{HC}$ = 0.5 ms; $\tau_{NC}$ = 1.43 ms; $\nu_{1Hacq}$ = 71 kHz | 20 hrs |
| | 2D NC TEDOR | $B_0$ = 18.8 T; $T_{bearing}$ = 263 K; $\nu_{MAS}$ = 14 kHz, ns = 256, $\tau_{rd}$ = 2.0 s, $t_{1,max}$ = 10 ms; $t_{1,inc}$ = 142.9 µs; $\tau_{dwell}$ = 6 µs; $\tau_{acq}$ = 12.3 ms; $\tau_{HC}$ = 0.5 ms; $\tau_{NC}$ = 1.43 ms; $\nu_{1Hacq}$ = 71 kHz | 20 hrs |
| | | | |

| | | | |
|---|---|---|---|
| pH 7.5, DMPX, HMA : ETM (4 : 1) | 2D CC short CORD | $B_0$ = 18.8 T; $T_{bearing}$ = 305 K; $\nu_{MAS}$ = 14 kHz, ns = 96, $\tau_{rd}$ = 1.6 s, $t_{1,max}$ = 6.2 ms; $t_{1,inc}$ = 25.0 µs; $\tau_{dwell}$ = 6.0 µs; $\tau_{acq}$ = 12.2 ms; $\tau_{HC}$ = 0.5 ms; $\tau_{CORD}$ = 20 ms; $\nu_{1Hacq}$ = 71 kHz | 17 hrs |
| | 2D NC TEDOR | $B_0$ = 18.8 T; $T_{bearing}$ = 305 K; $\nu_{MAS}$ = 14 kHz, ns = 224, $\tau_{rd}$ = 2.0 s, $t_{1,max}$ = 10 ms; $t_{1,inc}$ = 142.9 µs; $\tau_{dwell}$ = 6 µs; $\tau_{acq}$ = 12.3 ms; $\tau_{HC}$ = 0.5 ms; $\tau_{NC}$ = 1.43 ms; $\nu_{1Hacq}$ = 71 kHz | 17 hrs |
| pH 7.5 DMPX Amt : ETM (8 : 1) | 1D $^{19}$F DP | $B_0$ = 14.1 T; $T_{bearing}$ = 270 K; $\nu_{MAS}$ = 14 kHz, ns = 10240, $\tau_{rd}$ = 1.5 s, $\tau_{dwell}$ = 6 µs; $\tau_{acq}$ = 6.1 ms; $\nu_{1Hacq}$ = 71 kHz | 4.3 hrs |
| | 1D broadband $^{13}$C-$^{19}$F REDOR, 9.1 ms (S and $S_0$ pair) | $B_0$ = 14.1 T; $T_{bearing}$ = 270 K; $\nu_{MAS}$ = 14 kHz, ns = 5120, $\tau_{rd}$ = 1.8 s, $\tau_{dwell}$ = 8 µs; $\tau_{acq}$ = 6.1 ms; $\tau_{HC}$ = 0.5 ms; $\tau_{CFREDOR}$=9.1 ms; $\nu_{1HREDOR}$ = 117 kHz; $\nu_{1Hacq}$ = 71 kHz | 5.2 hrs |
| | 1D broadband $^{13}$C-$^{19}$F REDOR, 11.4 ms (S and $S_0$ pair) | $B_0$ = 14.1 T; $T_{bearing}$ = 270 K; $\nu_{MAS}$ = 14 kHz, ns = 5120, $\tau_{rd}$ = 1.8 s, $\tau_{dwell}$ = 8 µs; $\tau_{acq}$ = 6.1 ms; $\tau_{HC}$ = 0.5 ms; $\tau_{CFREDOR}$=11.4 ms; $\nu_{1HREDOR}$ = 117 kHz; $\nu_{1Hacq}$ = 71 kHz | 5.2 hrs |
| | 1D Cα-selective $^{13}$C-$^{19}$F REDOR, 10.0 ms (S and $S_0$ pair) | $B_0$ = 14.1 T; $T_{bearing}$ = 270 K; $\nu_{MAS}$ = 14 kHz, ns = 5120, $\tau_{rd}$ = 1.8 s, $\tau_{dwell}$ = 8 µs; $\tau_{acq}$ = 6.1 ms; $\tau_{13Cαsel}$ = 286 µs; $\tau_{HC}$ = 0.5 ms; $\tau_{CFREDOR}$=10.0 ms; $\nu_{1HREDOR}$ = 117 kHz; $\nu_{1Hacq}$ = 71 kHz | 5.2 hrs |
| | 1D Cα-selective $^{13}$C-$^{19}$F REDOR, 14.3 ms (S and $S_0$ pair) | $B_0$ = 14.1 T; $T_{bearing}$ = 270 K; $\nu_{MAS}$ = 14 kHz, ns = 5120, $\tau_{rd}$ = 1.8 s, $\tau_{dwell}$ = 8 µs; $\tau_{acq}$ = 6.1 ms; $\tau_{13Cαsel}$ = 286 µs; $\tau_{HC}$ = 0.5 ms; $\tau_{CFREDOR}$=14.3 ms; $\nu_{1HREDOR}$ = 117 kHz; $\nu_{1Hacq}$ = 71 kHz | 5.2 hrs |
| | 2D CC short CORD | $B_0$ = 18.8 T; $T_{bearing}$ = 263 K; $\nu_{MAS}$ = 14 kHz, ns = 96, $\tau_{rd}$ = 1.6 s, $t_{1,max}$ = 6.2 ms; $t_{1,inc}$ = 25.0 µs; $\tau_{dwell}$ = 6.0 µs; $\tau_{acq}$ = 12.2 ms; $\tau_{HC}$ = 0.5 ms; $\tau_{CORD}$ = 20 ms; $\nu_{1Hacq}$ = 71 kHz | 17 hrs |
| | 2D NC TEDOR | $B_0$ = 18.8 T; $T_{bearing}$ = 305 K; $\nu_{MAS}$ = 14 kHz, ns = 256, $\tau_{rd}$ = 2.0 s, $t_{1,max}$ = 10 ms; $t_{1,inc}$ = 142.9 µs; $\tau_{dwell}$ = 6 µs; $\tau_{acq}$ = 12.3 ms; $\tau_{HC}$ = 0.5 ms; $\tau_{NC}$ = 1.43 ms; $\nu_{1Hacq}$ = 71 kHz | 20 hrs |
| pH 5.0, DMPX No Salt | 2D CC short CORD | $B_0$ = 18.8 T; $T_{bearing}$ = 305 K; $\nu_{MAS}$ = 14 kHz, ns = 96, $\tau_{rd}$ = 1.6 s, $t_{1,max}$ = 6.2 ms; $t_{1,inc}$ = 25.0 µs; $\tau_{dwell}$ = 10.0 µs; $\tau_{acq}$ = 12.2 ms; $\tau_{HC}$ = 0.5 ms; $\tau_{CORD}$ = 20 ms; $\nu_{1Hacq}$ = 71 kHz | 17 hrs |
| pH 5.0, DMPX 5 mM $CaCl_2$ | 2D CC short CORD | $B_0$ = 18.8 T; $T_{bearing}$ = 305 K; $\nu_{MAS}$ = 14 kHz, ns = 96, $\tau_{rd}$ = 1.6 s, $t_{1,max}$ = 6.2 ms; $t_{1,inc}$ = 25.0 µs; $\tau_{dwell}$ = 10.0 µs; $\tau_{acq}$ = 12.2 ms; $\tau_{HC}$ = 0.5 ms; $\tau_{CORD}$ = 20 ms; $\nu_{1Hacq}$ = 71 kHz | 17 hrs |
| | 2D NC TEDOR | $B_0$ = 18.8 T; $T_{bearing}$ = 305 K; $\nu_{MAS}$ = 14 kHz, ns = 224, $\tau_{rd}$ = 2.0 s, $t_{1,max}$ = 10 ms; $t_{1,inc}$ = 142.9 µs; $\tau_{dwell}$ = 6 µs; $\tau_{acq}$ = 12.3 ms; $\tau_{HC}$ = 0.5 ms; $\tau_{NC}$ = 1.43 ms; $\nu_{1Hacq}$ = 71 kHz | 17 hrs |

Definitions of symbols: $B_0$ = magnetic field; $T_{bearing}$ = thermocouple-reported bearing gas temperature; $\nu_{MAS}$ = MAS frequency; ns = number of scans per free induction decay; $\tau_{rd}$ = recycle delay; $t_{1,max}$ = maximum $t_1$ evolution time; $t_{1,inc}$ = $t_1$ increment; $t_{2,max}$ = maximum $t_2$ evolution time; $t_{2,inc}$ = $t_2$ increment; $\tau_{dwell}$ = dwell-time in the direct dimension; $\tau_{acq}$ = maximum acquisition time in the direct dimension; $\tau_{HC}$ = $^1$H-$^{13}$C cross polarization contact time; $\tau_{CORD}$ = $^{13}$C-$^{13}$C mixing time using CORD; $\nu_{1Hacq}$ = $^1$H rf field strength for decoupling during acquisition; $\tau_{NC}$ = total $^{15}$N-$^{13}$C TEDOR recoupling time; $\tau_{HN}$ = $^1$H-$^{15}$N cross polarization contact time; $\tau_{1Hexc}$ = $^1$H 90° pulse length for selective excitation of water; $\tau_{1HSD}$ = $^1$H-$^1$H spin diffusion mixing time; $\tau_{13Cαsel}$ = 180° pulse length for selective inversion of Cα resonances; $\tau_{CFREDOR}$ = total $^{13}$C-$^{19}$F REDOR recoupling time; $\nu_{1HREDOR}$ = $^1$H rf field strength for decoupling during $^{13}$C-$^{19}$F REDOR.

# Figures

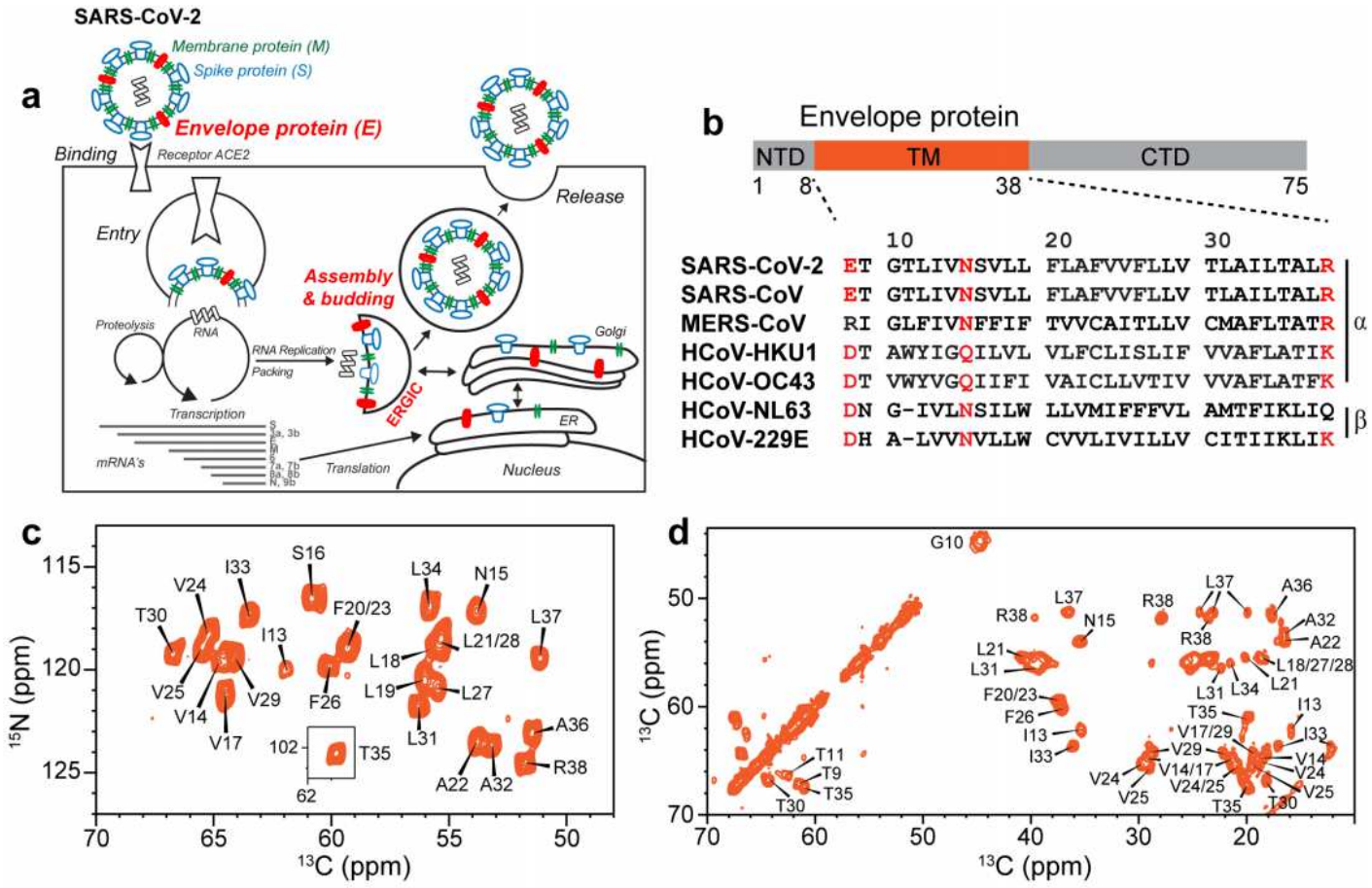


**Figure 1**

Function, sequence, and fingerprint NMR spectra of the SARS-CoV-2 envelope protein. (a) E mediates the budding and release of SARS-CoV-2 from the host cell ERGIC lumen and forms a cation-selective channel. (b) Sequence domains of E and sequence alignment of the transmembrane segment of E of SARS-CoV-2 with other human-infecting coronaviruses. Key conserved polar residues are shown in red. (c) 2D 15N13Cα correlation spectrum and (d) 2D 13C- 13C spectrum of ERGIC-membrane bound ETM. The spectra, measured at ambient temperature, show predominantly α-helical chemical shifts, and have high sensitivity and resolution, indicating that the ETM helical bundle is rigid and ordered in the ERGIC-mimetic lipid bilayer.

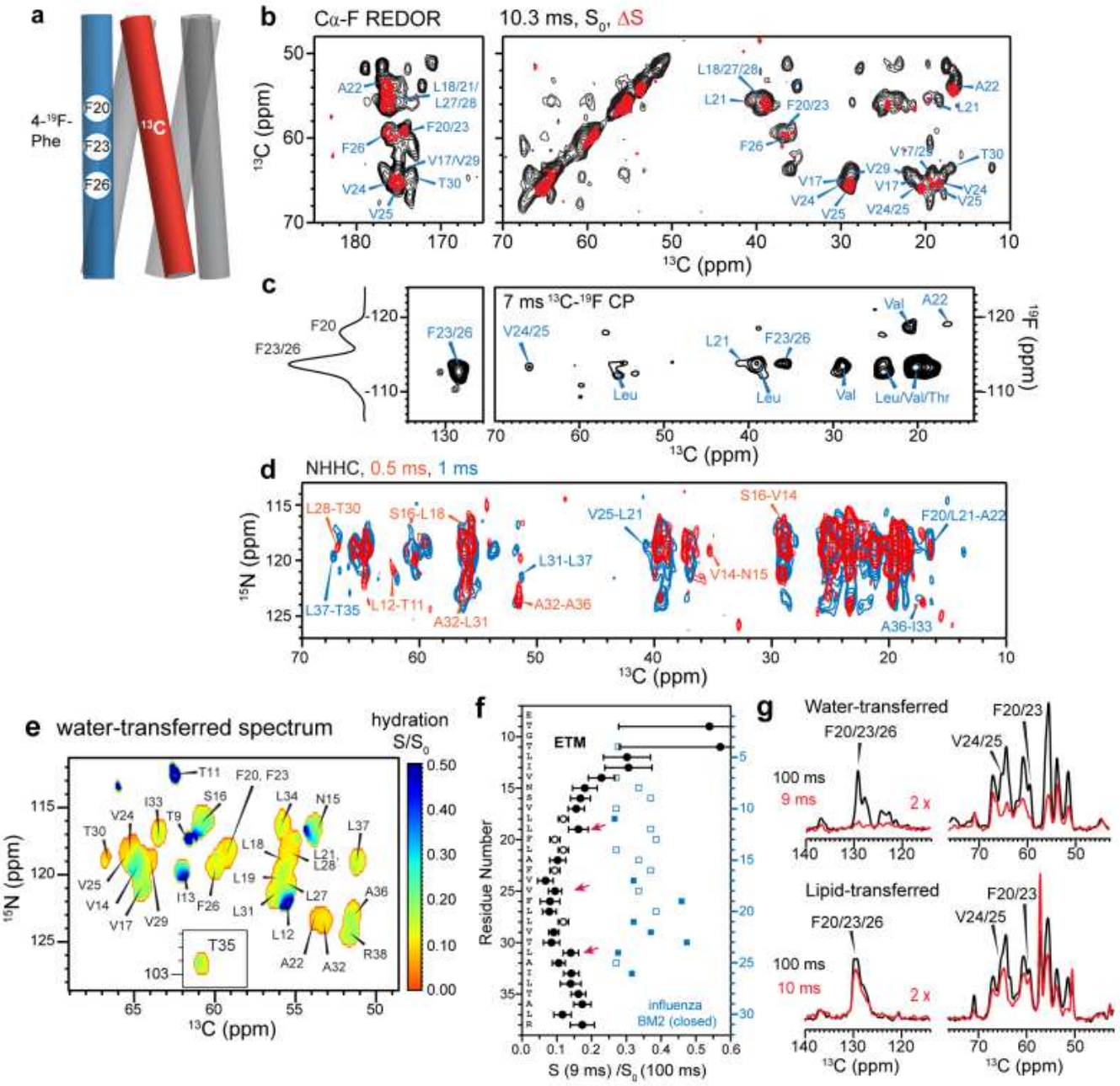


## Figure 2

Determination of interhelical distances and water accessibility of membrane-bound ETM. (a) Schematic of mixed 4F-Phe and 13C-labeled ETM in a five-helix bundle. (b) 2D 13Ca-F REDOR spectra of ERGIC-membrane bound ETM. The REDOR mixing time was 10.3 ms. The difference spectrum (orange) shows residues that are close to the fluorines. (c) 2D 13C19F correlation spectrum allows assignment of the -118 ppm peak to F20 due to a cross peak with A22, while the -113 ppm peak is assigned to F23/F26 based on correlations with F23, F26, and V24/V25. A 1D 1 H19F CP spectrum is overlaid on the left. (d) 2D NHHC correlation spectrum of mixed 13C and 15N labeled ETM, measured using 0.5 ms (red) and 1 ms (black) 1 H mixing. All peaks arise from interhelical contacts. Selected assignments are given. (e) Residue-specific water accessibilities of ERGIC-bound ETM, obtained from the intensity ratios of water-edited spectra measured with 9 ms and 100 ms 1 H mixing. Higher values (blue) indicate higher water

accessibility. (f) Residue-specific N-Ca cross peak intensity ratios in the 9 ms and 100 ms wateredited spectra of ETM (black). Closed and open circles indicate resolved and overlapped peaks, respectively. For comparison, the water-edited intensities for the high-pH closed state of the influenza BM2 channel (blue squares) are much higher, indicating that the ETM pore is drier than the BM2 pore. (g) Water-edited and lipid-edited 1D 13C spectra of ERGIC-membrane bound ETM. The Phe signals are high in the lipid-edited spectra but very low in the water-edited spectra, indicating that the three Phe residues are poorly hydrated and point to the lipids or the helix-helix interface.

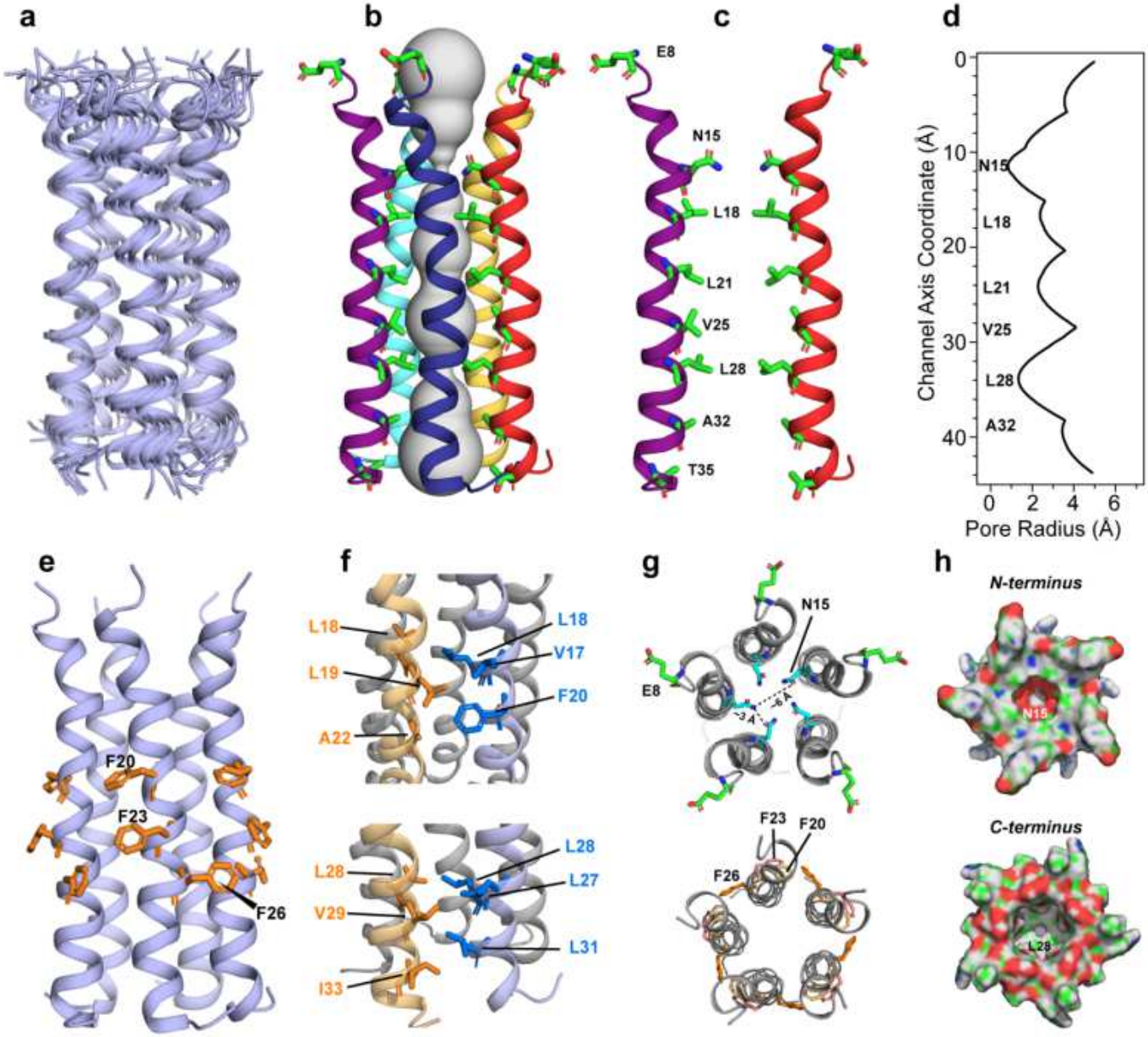


## Figure 3

Structure of the SARS-CoV-2 envelope protein TM domain in ERGIC-mimetic lipid bilayers. (a) Ensemble of the ten lowest-energy structures. (b) Sideview of the lowest-energy structure along with pore water (gray), depicted using the HOLE program. Pore-lining residues are shown in sticks. (c) Simplified view

showing two helices (i and i+2) with the pore-facing residues. (d) Pore radius of ETM obtained from the HOLE program. (e) Sideview of the pentamer, displaying the Phe triplet in the middle of the TM segment. (f) Two clusters of methyl-interdigitating Leu, Ile and Val residues, stabilizing the helix-helix interface. (g) Top views of the disordered Nterminal E8, the pore-occluding N15, and the three Phe residues bridging the helix-helix interface. (h) Surface plots of the pentamer, showing that the N-terminal vestibule is slightly tighter than the C-terminal opening.

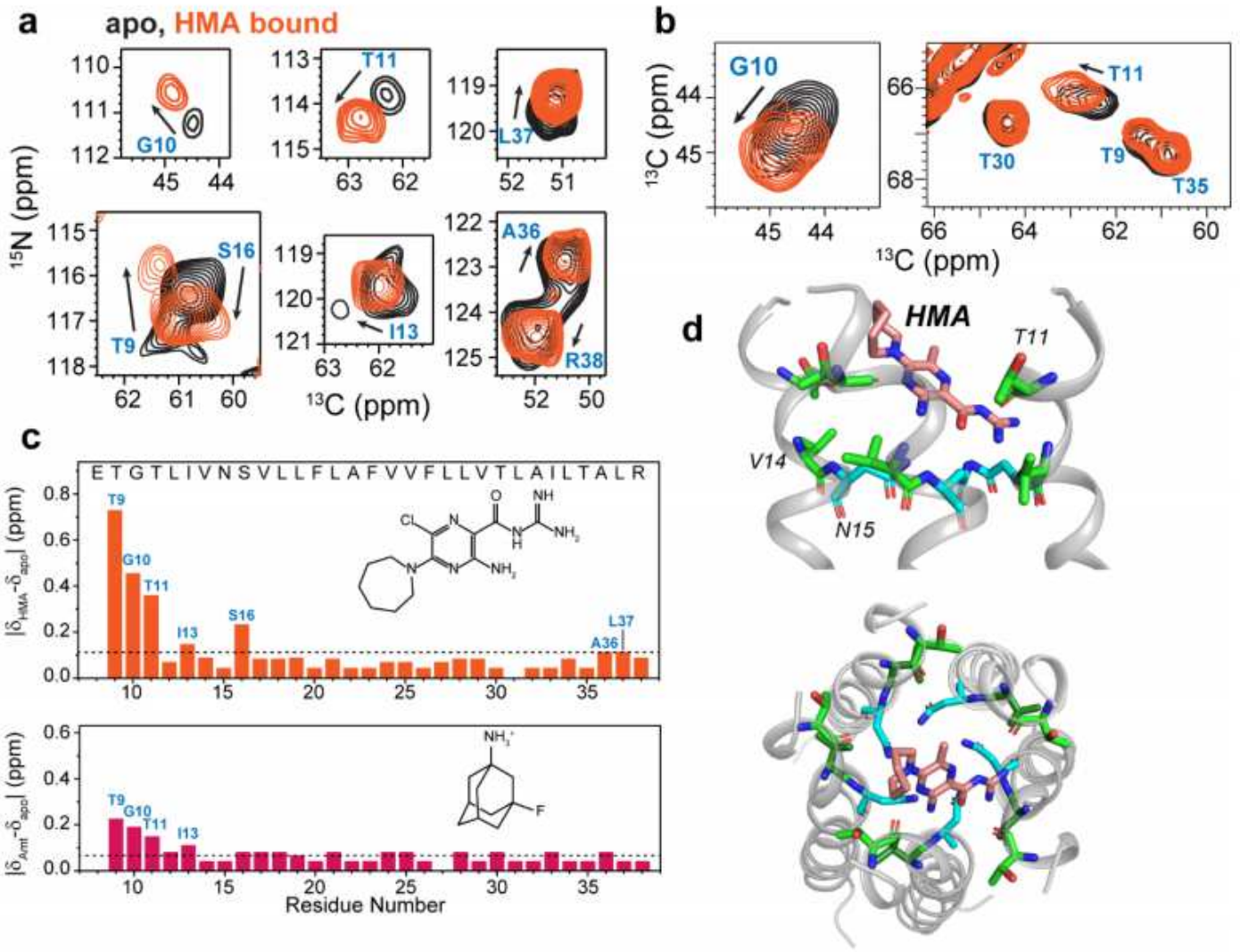


**Figure 4**

Effects of drug binding to ETM in DMPC : DMPG membranes. (a) 2D 15N13Cα correlation spectra of the apo (black) and HMA-bound ETM (orange), showing chemical shift perturbations by HMA. (c) 2D 13C13C correlation spectra, showing similar CSPs by HMA. (c) Perresidue chemical shift perturbations induced by HMA and AMT. N-terminal residues are the most perturbed by both drugs, and HMA causes larger perturbation than AMT. Dashed lines indicate the average CSPs. (d) A representative docking pose of HMA. The drug binds to the N-terminal vestibule, with the guanidinium group interacting with T11.

## Supplementary Files

This is a list of supplementary files associated with this preprint. Click to download.

- D1000251802valreportfullannotateP1.pdf